

---

**Abstract**

*Key words:*

---

**1.**

**References**

□

---

**Abstract**

*Key words:*

---

**1.**

**References**

[1]

# Particle Flow Calorimetry and the PandoraPFA Algorithm

M. A. Thomson

*Cavendish Laboratory, JJ Thomson Avenue, Cambridge CB3 0HE, United Kingdom.*

---

## Abstract

The Particle Flow (PFlow) approach to calorimetry promises to deliver unprecedented jet energy resolution for experiments at future high energy colliders such as the proposed International Linear Collider (ILC). This paper describes the PandoraPFA particle flow algorithm which is then used to perform the first systematic study of the potential of high granularity PFlow calorimetry. For simulated events in the ILD detector concept, a jet energy resolution of  $\sigma_E/E \lesssim 3.8\%$  is achieved for 40 – 400 GeV jets. This result, which demonstrates that high granularity PFlow calorimetry can meet the challenging ILC jet energy resolution goals, does not depend strongly on the details of the Monte Carlo modelling of hadronic showers. The PandoraPFA algorithm is also used to investigate the general features of a collider detector optimised for high granularity PFlow calorimetry. Finally, a first study of the potential of high granularity PFlow calorimetry at a multi-TeV lepton collider, such as CLIC, is presented.

*Key words:* Particle Flow Calorimetry, Calorimetry, ILC

*PACS:* 07.05.Kf, 29.40.Vj.+c

---

## 1. Introduction

In recent years the concept of high granularity Particle Flow calorimetry [1] has been developed in the context of the proposed International Linear Collider (ILC). Many of the interesting physics processes at the ILC [2] will be characterised by multi-jet final states, often accompanied by charged leptons and/or missing transverse energy associated with neutrinos or the lightest super-symmetric particles. The reconstruction of the invariant masses of two or more jets will provide a powerful tool for event reconstruction and event identification. Unlike at LEP, where kinematic fitting [3] enabled precise invariant mass reconstruction, at the ILC di-jet mass reconstruction will rely on the jet energy resolution of the detector. The goal for jet energy resolution at the ILC is that it is sufficient to cleanly separate W and Z hadronic decays. An invariant mass resolution comparable to the gauge boson widths, *i.e.*  $\sigma_m/m = 2.7\% \approx \Gamma_W/m_W \approx \Gamma_Z/m_Z$ , leads to an effective  $3.6\sigma$  separation of the  $W \rightarrow q'\bar{q}$  and  $Z \rightarrow q\bar{q}$  mass peaks, *i.e.* the optimal invariant mass cut corresponds to  $+1.8\sigma$  ( $-1.8\sigma$ ) in the reconstructed W (Z) mass distributions.

---

*Email address:* thomson@hep.phy.cam.ac.uk (M. A. Thomson)

In the traditional calorimetric approach, the jet energy is obtained from the sum of the energies deposited in the electromagnetic and hadronic calorimeters (ECAL and HCAL). This typically results in a jet energy resolution of the form

$$\frac{\sigma_E}{E} = \frac{\alpha}{\sqrt{E(\text{GeV})}} \oplus \beta. \quad (1)$$

The stochastic term,  $\alpha$ , is usually greater than  $\sim 60\%$ . The constant term,  $\beta$ , which encompasses a number of effects, is typically a few per cent. For high energy jets there also will be a contribution from the non-containment of the hadronic showers. The stochastic term in the jet energy resolution results in a contribution to the di-jet mass resolution of  $\sigma_m/m \approx \alpha/\sqrt{E_{jj}}$ , where  $E_{jj}$  is the energy of the di-jet system in GeV. At the ILC, operating at centre-of-mass energies  $\sqrt{s} = 0.5 - 1.0 \text{ TeV}$ , the typical di-jet energies for interesting physics processes will be in the range  $150 - 350 \text{ GeV}$ . Hence to achieve the ILC goal of  $\sigma_m/m = 2.7\%$ , the stochastic term must be  $\lesssim 30\%/\sqrt{E(\text{GeV})}$ . This is unlikely to be achievable with a traditional approach to calorimetry.

### 1.1. The Particle Flow Approach to Calorimetry

Measurements of jet fragmentation at LEP have provided detailed information on the particle composition of jets (*e.g.* [4, 5]). On average, after the decay of short-lived particles, roughly 62% of the jet energy is carried by charged particles (mainly hadrons), around 27% by photons, about 10% by long-lived neutral hadrons (*e.g.*  $n$ ,  $\bar{n}$  and  $K_L$ ), and around 1.5% by neutrinos. Hence, approximately 72% of the jet energy is measured in the HCAL and the jet energy resolution is limited by the relatively poor HCAL energy resolution, typically  $\gtrsim 55\%/\sqrt{E(\text{GeV})}$ . The LEP collaborations, most notably ALEPH, and other collider experiments (*e.g.* H1, D0 and CMS) have obtained improved jet energy resolution using the Energy Flow [6] approach, whereby energy deposits in the calorimeters are removed according to the momentum of the charged particle tracks. Using this method, ALEPH achieved a jet energy resolution (for  $\sqrt{s} = M_Z$ ) equivalent to  $\sigma_E/E \approx 65\%/\sqrt{E(\text{GeV})}$  [6]. This is the best jet energy resolution of the four LEP experiments, but is roughly a factor two worse than required for the ILC.

It is widely believed that the most promising strategy<sup>1</sup> for achieving the ILC jet energy goal is the Particle Flow (PFlow) approach to calorimetry. This extends the concept of Energy Flow to a highly granular detector. In contrast to a purely calorimetric measurement, PFlow calorimetry requires the reconstruction of the four-vectors of all visible particles in an event. The reconstructed jet energy is the sum of the energies of the individual particles. The momenta of charged particles are measured in the tracking detectors, while the energy measurements for photons and neutral hadrons are obtained from the calorimeters. In this manner, the HCAL is used to measure only  $\sim 10\%$  of the energy in the jet. If one were to assume calorimeter resolutions of  $\sigma_E/E = 0.15/\sqrt{E(\text{GeV})}$  for photons and  $\sigma_E/E = 0.55/\sqrt{E(\text{GeV})}$  for hadrons, a jet energy resolution of  $0.19/\sqrt{E(\text{GeV})}$  would be obtained with the contributions from tracks, photons and neutral hadrons as given in Table 1. In practice, this level of performance can not be achieved as it is not possible to perfectly associate all energy deposits with the correct particles. For example, if the calorimeter hits from a photon are not resolved from a charged hadron shower, the photon energy is not accounted for. Similarly, if part of charged hadron shower is identified as a separate cluster, the energy is effectively double-counted as it is already accounted for by

---

<sup>1</sup>The only alternative proposed to date is that of Dual Readout calorimetry as studied by the DREAM collaboration [7].

the track momentum. This *confusion* rather than calorimetric performance is the limiting factor in PFlow calorimetry. Thus, the crucial aspect of PFlow calorimetry is the ability to correctly assign calorimeter energy deposits to the correct reconstructed particles. This places stringent requirements on the granularity of the ECAL and HCAL. From the point of view of event reconstruction, the sum of calorimeter energies is replaced by a complex pattern recognition problem, namely the Particle Flow reconstruction Algorithm (PFA). The jet energy resolution obtained is a combination of the intrinsic detector performance and the performance of the PFA software.

Component	Detector	Energy Fract.	Energy Res.	Jet Energy Res.
Charged Particles ( $X^\pm$ )	Tracker	$\sim 0.6 E_j$	$10^{-4} E_{X^\pm}^2$	$< 3.6 \times 10^{-5} E_j^2$
Photons ( $\gamma$ )	ECAL	$\sim 0.3 E_j$	$0.15 \sqrt{E_\gamma}$	$0.08 \sqrt{E_j}$
Neutral Hadrons ( $h^0$ )	HCAL	$\sim 0.1 E_j$	$0.55 \sqrt{E_{h^0}}$	$0.17 \sqrt{E_j}$

Table 1: Contributions from the different particle components to the jet-energy resolution (all energies in GeV). The table lists the approximate fractions of charged particles, photons and neutral hadrons in a jet of energy,  $E_j$ , and the assumed single particle energy resolution.

The PandoraPFA algorithm was developed to study PFlow calorimetry at the ILC. PandoraPFA is a C++ implementation of a PFA running in the MARLIN [8] reconstruction framework. It was developed and optimised using simulated physics events generated with the MOKKA [9] program, which provides a detailed Geant4 [10] simulation of potential detector concepts for the ILC. In particular, PandoraPFA was developed using the MOKKA simulation of the LDC [11] detector concept and, more recently, the ILD [12] detector concept. The algorithm is designed to be sufficiently flexible to allow studies of PFlow for different detector designs. Whilst a number of PFAs [13, 14, 15] have been developed for the ILC, PandoraPFA is the most sophisticated and best performing algorithm. In this paper PandoraPFA is described in detail. It is then used to study the potential at a future high energy lepton collider of PFlow calorimetry with a highly granular detector, in this case the ILD detector concept.

## 2. Overview of the ILD Detector Model

The ILD detector concept [12], shown in Figure 1, consists of a vertex detector, tracking detectors, ECAL, HCAL and muon chambers. It represents a possible configuration of a detector suitable for PFlow calorimetry. Specifically, for the ECAL and HCAL the emphasis is on granularity, both longitudinal and transverse, rather than solely energy resolution. Suitable candidate technologies are being studied by the CALICE (calorimetry for the ILC) collaboration [16]. Amongst these are the Silicon-Tungsten ECAL and Steel-Scintillator HCAL designs assumed for the baseline ILD detector simulation.

Both the ECAL and HCAL are located inside a solenoid which is taken to produce the 3.5 T magnetic field. The main tracking detector is simulated as a time projection chamber (TPC) with an active gas volume of half-length 2.25 m and inner and outer radii of 0.39 m and 1.74 m respectively. The vertex detector consists of 6 layers of Silicon with an inner radius of 15 mm from the interaction point (IP). The tracking is complemented by two barrel Silicon strip detectors between the vertex detector and the TPC and seven Silicon forward tracking disks. The ECAL is simulated as a Silicon-Tungsten sampling calorimeter consisting of 29 layers. The first 20 layers

have 2.1 mm thick Tungsten and the last 9 layers have 4.2 mm thick Tungsten. The high resistivity Silicon is segmented into  $5 \times 5 \text{ mm}^2$  pixels. At normal incidence, the ECAL corresponds to 23 radiation lengths ( $X_0$ ) and 0.8 nuclear interaction lengths ( $\lambda_I$ ). The HCAL is simulated as a Steel-Scintillator sampling calorimeter comprising 48 layers of 20 mm thick Steel and 5 mm thick  $3 \times 3 \text{ cm}^2$  plastic scintillator tiles. At normal incidence the HCAL is  $6 \lambda_I$  thick.

The ECAL and HCAL in the ILD concept are well matched to the requirements of PFlow calorimetry. Tungsten is the ideal absorber material for the ECAL; it has a short radiation length and small Molière radius (see Table 2) which leads to compact electromagnetic (EM) showers. It also has a large ratio of interaction length to radiation length which means that hadronic showers will tend to be longitudinally well separated from EM showers. The  $5 \times 5 \text{ mm}^2$  transverse segmentation takes full advantage of the small Molière radius. Steel is chosen as the HCAL absorber, primarily for its structural properties. The  $3 \times 3 \text{ cm}^2$  HCAL transverse segmentation is believed to be well matched to the requirements of PFlow calorimetry (see Section 9.5).

Material	$\lambda_I/\text{cm}$	$X_0/\text{cm}$	$\rho_M/\text{cm}$	$\lambda_I/X_0$
Fe	16.8	1.76	1.69	9.5
Cu	15.1	1.43	1.52	10.6
W	9.6	0.35	0.93	27.4
Pb	17.1	0.56	1.00	30.5

Table 2: Comparison of interaction length,  $\lambda_I$ , radiation length,  $X_0$ , and Molière radius,  $\rho_M$ , for Iron, Copper, Tungsten and Lead. Also given is the ratio of  $\lambda_I/X_0$ .

### 3. Reconstruction Framework

The performance of PFlow calorimetry depends strongly on the reconstruction software. For the results obtained to be meaningful, it is essential that both the detector simulation and the reconstruction chain are as realistic as possible. For this reason no Monte Carlo (MC) information is used at any stage in the reconstruction as this is likely to lead to an overly-optimistic evaluation of the potential performance of PFlow calorimetry.

PandoraPFA runs in the MARLIN [8] C++ framework developed for the LDC and ILD detector concepts. The input to PandoraPFA (in LCIO [17] format) is a list of digitised hits in the calorimeters and a list of reconstructed tracks. Tracks in the TPC are reconstructed using a MARLIN processor, LEPTackingProcessor, adapted from the TPC pattern recognition software [18] based on that used by ALEPH and track fitting software used by DELPHI [19]. Reconstruction of tracks in the inner Silicon detectors is performed by a custom processor, SiliconTracking [21]. TPC and Silicon track segments are combined in a final tracking processor, FullLDCTracking [21].

PandoraPFA combines the tracking information with hits in the high granularity calorimeters to reconstruct the individual particles in the event. As an example of the information used in the reconstruction, Figure 2 shows a photon, a charged hadron ( $\pi^+$ ) and a neutral hadron ( $K_L$ ) as simulated in the ILD detector concept.

## 4. The PandoraPFA Particle Flow Algorithm

The PandoraPFA algorithm performs calorimeter clustering and PFlow reconstruction in eight main stages: 1) *Track Selection/Topology*: track topologies such as kinks and decays of neutral particles in the detector volume (e.g.  $K_S \rightarrow \pi^+\pi^-$ ) are identified. 2) *Calorimeter Hit Selection and Ordering*: isolated hits, defined on the basis of proximity to other hits, are removed from the initial clustering stage. The remaining hits are ordered into *pseudo-layers* and information related to the geometry and the surrounding hits are stored for use in the reconstruction. 3) *Clustering*: the main clustering algorithm is a cone-based forward projective method [22] working from innermost to outermost pseudo-layer. The algorithm starts by seeding clusters using the projections of reconstructed tracks onto the front face of the ECAL. 3A) *Photon Clustering*: PandoraPFA can be run in a mode where the above clustering algorithm is performed in two stages. In the first stage, only ECAL hits are considered with the aim of identifying energy deposits from photons. In the second stage the clustering algorithm is applied to the remaining hits. 4) *Topological Cluster Merging*: by design the initial clustering stage errs on the side of splitting up true clusters rather than merging energy deposits from more than one particle into a single cluster. Clusters are then combined on the basis of clear topological signatures in the high granularity calorimeters. The topological cluster merging algorithms are only applied to clusters which have not been identified as photons. 5) *Statistical Re-clustering*: The previous four stages of the algorithm are found to perform well for jets with energies of less than 50 GeV. For higher energy jets the performance degrades due to the increasing overlap between hadronic showers from different particles. Clusters which are likely to have been created from the merging of hits in showers from more than one particle are identified on the basis of the compatibility of the cluster energy,  $E_C$ , and the associated track momentum,  $p$ . In the case of an inconsistent energy-momentum match, attempts are made to re-cluster the hits by re-applying the clustering algorithm with different parameters, until the cluster splits to give a cluster energy consistent with the momentum of the associated track. 6) *Photon Recovery and Identification*: A more sophisticated, shower-profile based, photon-identification algorithm is then applied to the clusters, improving the tagging of photons. It is also used to recover cases where a primary photon is merged with a hadronic shower from a charged particle. 7) *Fragment Removal*: “neutral clusters” which are *fragments* of charged particle hadronic showers are identified. 8) *Formation of Particle Flow Objects*: The final stage of the algorithm is to create the list of reconstructed particles, Particle Flow Objects (PFOs), and associated four-momenta.

The essential features of each of the above stages are described in more detail below. The description includes the main configuration parameters which determine the behaviour of the algorithms. These can be defined at runtime. The default values, which are optimised for the ILD concept, are given.

### 4.1. Track selection/topology

Tracks are projected onto the front face of the ECAL using a helical fit to the last 50 hits on the reconstructed track (no account is taken for energy loss along the trajectory in the TPC gas). Tracks are then classified according to their likely origin. For example, neutral particle decays resulting in two charged particle tracks ( $V^0$ s) are identified by searching for pairs of tracks which are consistent with coming from a single point displaced from the IP. Charged particle decays to a single charged particle and any number of neutral particles (kinks) are identified on the basis of the distance of closest approach of the parent and daughter tracks. Similarly, interactions in the tracking volume (prongs) are identified. This information, along with the

original track parameters and the projection of the track onto the front face of the ECAL, is stored in `ExtendedTrack` objects for use in the subsequent event reconstruction.

#### 4.2. Calorimeter Hit Selection and Ordering

In addition to the reconstructed tracks, the input to PandoraPFA is a list of digitised calorimeter hits. For each hit, the position  $(x, y, z)$ , the energy deposition, and the physical layer in the ECAL/HCAL are specified. Based on this information, `ExtendedCaloHit` objects are formed. These hits are self-describing and incorporate information relating to both the geometry of the detector (accessed from the GEAR[23] geometry description) and information related to the density of calorimeter hits in the neighbouring region. The five main steps in the calorimeter hit processing (calibration, geometry, isolation, MIP identification, ordering) are described below.

##### 4.2.1. Calibration

The energy of each calorimeter hit is converted to a minimum ionising particle (MIP) equivalent (at normal incidence) using a calibration factor `CALMIPcalibration`. Different calibration factors are used for ECAL and HCAL hits. Hits are only retained if they are above a MIP-equivalent threshold of `CalMIPThreshold` (with default values of [0.5] and [0.3] for ECAL and HCAL respectively). The MIP equivalent energy deposit is then converted into calorimetric measurement using MIP to GeV calibration factors, `CalMIPToGeV`, for the ECAL and HCAL. In general, the calorimeters will not be compensating, and separate energy measurements are calculated for the hypotheses that the hit is either part of an EM or hadronic shower. The final choice of which energy to use depends on the whether the shower to which a hit is associated is ultimately identified as being EM in nature. To allow for calorimeters with different absorber thicknesses as a function of depth, the calibration factor applied is proportional to the absorber thickness of the layer in front of the hit. Initial values for the calibration factors are determined from MC samples of single muons, photons and  $K_L$ s. The muon sample is used to determine the MIP calibration, the photon sample is used to determine the ECAL calibrations and the  $K_L$ s are used to determine the initial HCAL calibration. Since the neutral hadrons in jets are a mixture of  $K_L$ s, neutrons and anti-neutrons, the initial HCAL calibration is modified (typically by  $\sim 5\%$ ) on the basis of minimising the jet energy resolutions for MC samples of jets. A single set of calibration factors is used for the subsequent studies.

##### 4.2.2. Geometry information

The PandoraPFA reconstruction is designed to minimise the dependence on the detector geometry to enable comparisons of different detector designs. For this reason, information is added to the digitised calorimeter hits such that they become self describing. For example, the `ExtendedCaloHit` objects store the size of the corresponding detector pixel. To reduce the dependency of the clustering algorithms on the detector geometry, hits are ordered in increasing depth in the calorimeter. This is achieved by defining “pseudo-layers” which follow the general layer structure of the calorimeters. This is necessary for calorimeter layouts such as in the ECAL stave-like structure being studied by the CALICE collaboration, shown schematically in Figure 3. Here there are regions where the first layer in a calorimeter stave can be deep in the overall calorimeter structure.



#### 4.2.3. Isolation Requirements

Low energy neutrons produced in hadronic showers can travel a significant distance from the point of production and thus produce isolated energy deposits. For PFlow calorimetry, these energy deposits are of little use as it is impossible to unambiguously associate them with a particular hadronic shower. For this reason, and to improve the performance of the clustering algorithms, isolated hits are identified and excluded from the initial cluster finding. Isolated hits are defined using one of two possible criteria: i) less than a minimum number of calorimeter hits within a pre-defined distance from the hit in question; or ii) a cut on the local weighted hit number density,  $\rho_i$ , defined by:

$$\rho_i = \sum_j w_{ij} = \sum_j \frac{1}{(r_{ij}^\perp)^n}$$

$$\text{where } r_{ij}^\perp = \frac{\mathbf{r}_i \times (\mathbf{r}_i - \mathbf{r}_j)}{|\mathbf{r}_i|}.$$

Here  $\mathbf{r}_i$  is the position of the hit in question, the sum over  $j$  is for all hits within a certain number of pseudo-layers of hit  $i$ , and the default value for  $n$  is 2. By default, method i) is used.

#### 4.2.4. MIP Identification

Hits which are consistent with having originated from a minimum ionising particle (MIP) are flagged based on energy deposition and the surrounding hits in the same calorimeter layer. For a hit to be tagged as MIP-like: a) the energy deposition must be no more than `MipLikeMipCut` [5.0] times the mean expected MIP signal, and b) of the adjacent (usually 8) pixels in the same layer, no more than `MipMaxCellsHit` [1] should have hits above threshold. This information is used in the identification of minimum ionising tracks within the calorimeter.

#### 4.2.5. Hit Ordering

Prior to applying the clustering algorithm, hits within each pseudo-layer are ordered either by energy (the default) or by local hit density,  $\rho_i$ , defined above. The latter option is intended primarily to be used for the case of digital calorimetry, where a simple hit count replaces the analogue energy information.

### 4.3. Clustering

The main clustering algorithm of PandoraPFA is a cone-based forward projective method working from innermost to outermost pseudo-layer. In this manner hits are either added to existing clusters or they are used to seed new clusters. Throughout the algorithm clusters are assigned a direction (or potentially directions) in which they are propagating. This allows the clustering algorithm to follow tracks in the calorimeters. The input to the clustering algorithm is a vector of hits (`ExtendedCaloHits`) ordered by pseudo-layer and energy (or local hit density) and a vector of tracks (`ExtendedTracks`).

The algorithm starts by *seeding* clusters using the projections of reconstructed tracks onto the front face of the ECAL. The initial direction of a track-seeded cluster is obtained from the track direction at the ECAL front face. The hits in each subsequent pseudo-layer are then looped over. Each hit,  $i$ , is compared to each clustered hit,  $j$ , in the previous layer. The vector displacement,  $\mathbf{r}_{ij}$ , is used to calculate the parallel and perpendicular displacement of the hit with respect to the unit vector(s)  $\hat{\mathbf{u}}$  describing the cluster propagation direction(s),  $d_{\parallel} = \mathbf{r}_{ij} \cdot \hat{\mathbf{u}}$  and  $d_{\perp} = |\mathbf{r}_{ij} \times \hat{\mathbf{u}}|$ . Associations are made using a cone-cut,  $d_{\perp} < d_{\parallel} \tan A + bD_{\text{pad}}$ , where  $A$  is the cone half-angle,  $D_{\text{pad}}$  is

the size of a sensor pixel in the layer being considered, and  $b$  is the number of pixels added to the cone radius. Different values of  $A$  and  $b$  are used for the ECAL and HCAL with the default values set to  $\{\tan A_E = 0.3, b_E = 1.5\}$  and  $\{\tan A_H = 0.5, b_H = 2.5\}$  respectively. The values can be modified using the steering parameters `ClusterFormationAngle` and `ClusterFormationPads`. For hits in layer  $k$ , associations are first searched for in layer  $k - 1$ . If no association is made, possible associations with clustered hits in layers  $k - 2$  and  $k - 3$  are considered in turn. If still no association is made, associations can be made with nearby hits in existing clusters in the same pseudo-layer as the hit in question, providing the distance between the hit centres is less than `SameLayerPadCut` = `[2.8]` (`[1.8]`) for pixels in the ECAL (HCAL). If a hit remains unassociated, it is used to seed a new cluster. Clusters seeded with calorimeter hits are assigned an initial direction corresponding to radial propagation from the IP. This procedure is repeated sequentially for the hits in each pseudo-layer working outward from ECAL front-face.

#### 4.3.1. Fast Photon Identification

Clusters which are consistent with being from EM showers from photons are identified. For reasons of speed, simple cut based criteria are used. The fast photon identification requirements<sup>2</sup> are: no associated track; the cluster must start within  $10 X_0$  of the front face of the ECAL; the cluster direction (obtained from a linear fit to the energy-weighted centroids of the hits in each pseudo-layer) must point to within  $20^\circ$  of the IP; the rms deviation of the hits in the cluster around the linear fit to the centroids in each calorimeter layer must be less than 40 cm; and the fraction of hits classified as MIP-like must be less than 30%. In addition, weak cuts on the longitudinal development of the shower are imposed. Photon clusters are essentially frozen at this stage in the PandoraPFA algorithm; they are not used in the subsequent topological cluster merging or reclustering algorithms.

#### 4.3.2. Photon Clustering (optional)

Rather than attempting to cluster all calorimeter hits in a single pass, PandoraPFA can be run in a mode (`PhotonClustering > 0`) where the clustering algorithm described above is first applied solely to the ECAL hits to identify photons as the first stage of PFlow reconstruction. The clustering algorithm parameters are chosen to reflect the narrowness of EM showers. Reconstructed clusters which are consistent with the expected EM transverse and longitudinal shower profiles (see Section 4.6) are stored and the associated calorimeter hits are not considered in the second pass of the clustering algorithm. The identified photon clusters are added back to the event just prior to the formation of the PFOs. For the results presented in this paper, photon clustering is run prior to the main clustering algorithm.

#### 4.4. Topological Cluster Merging

By design the initial clustering algorithm errs on the side of splitting up true clusters rather than merging energy deposits from more than one particle into a single cluster. Hence, the next stage in the PandoraPFA algorithm is to merge clusters which are not already associated to tracks (termed “neutral clusters”) with clusters which have an associated track (termed “charged clusters”). The merging algorithms are based on the clear topological signatures shown schematically in Figure 4.

---

<sup>2</sup>The exact cut values depend on the cluster energy and the values below are those given in the text are the default values for a 10 GeV cluster.

This procedure takes advantage of the high granularity of the ECAL and HCAL of a detector designed for PFlow reconstruction. For clusters with an associated track, the location of the first hadronic interaction is identified and the properties of the track-like segment in the calorimeter before the interaction are reconstructed. For neutral clusters, track-like segments are identified in the first and last six pseudo-layers of the cluster based on fraction of hits classified as MIP-like and the rms deviation of the hit positions about straight line fits. For track-like segments, the fitted line,  $\mathbf{r}_0 + \kappa \hat{\mathbf{d}}$ , is used to project forwards or backwards in the calorimeter. Similarly, the entire cluster may be classified as track-like. The main topological rules for cluster association are:

- (i) Looping tracks: Because of the forward projective nature of the primary clustering algorithm, tracks which turn back in the calorimeter due to the high magnetic field are often reconstructed as two track-like clusters. The track-like segments at the ends of the clusters are projected forwards and the clusters are combined if the distance of closest approach of the two forward-going track projections is less than `LooperClosestApproachCutECAL` [5 cm].
- (ii) Broken tracks: Non-continuous tracks in the calorimeters can arise when particles cross boundaries between physical sub-detectors or cross dead regions of the calorimeters. Such instances are identified using track-like segments in the last six layers of a charged cluster and the first six layers in a neutral cluster. The clusters may be merged if the distance of closest approach of the forward-going and backward-going track-like segment projections is less than `TrackMergeCutEcal` [2.5 cm].
- (iii) Tracks pointing to showers: If, when projected forward, a track-like charged cluster points to within `TrackMergeCutEcal` [2.5 cm] of the start of a cluster deeper in the calorimeter, the clusters may be merged.
- (iv) Track-like clusters pointing back to hadronic interactions: If the start of a neutral cluster is a track-like segment and it points to within `TrackBackMergeCut` [3.0 cm] of the identified first hadronic interaction of charged cluster, the clusters may be merged.
- (v) Back-scattered tracks: Hadronic interactions can produce tracks in the calorimeter which propagate backwards in the calorimeter. Due to the forward projective nature of the clustering algorithm, these often will be reconstructed as separate clusters. Back-scattered tracks are identified as track-like clusters which point to within `TrackBackMergeCut` [3.0 cm] of the identified hadronic interaction of a charged cluster.
- (vi) Hadronic interactions pointing to neutral clusters: If a charged-cluster has track-like segment prior to the identified interaction point, and it points to within `TrackForwardMergeCut` [5.0 cm] of the start of a cluster deeper in the calorimeter, the clusters may be merged.
- (vii) Proximity-based merging: The minimum distance between a charged cluster, of energy  $E_C$ , and a neutral cluster, of energy  $E_N$ , is defined as the smallest distance between any of the hits in the two clusters. If this distance is less than `ProximityCutDistance` [5 cm] then the clusters may be merged if there is additional evidence that the two clusters originate from a single hadronic shower. To suppress false matches the  $\chi^2$  consistency between the original and merged cluster energies and the associated track momentum,  $p$ , is used. The merged cluster energy,  $E' = E_C + E_N$ , must be consistent with the track momentum,  $\chi' = (E' - p)/\sigma_{E'}$  < `EnergyChi2ForCrudeMerging` [2.5], where  $\sigma_{E'}$  is the uncertainty on the merged cluster energy assuming that it is a hadronic shower. In addition, the  $\chi^2$  consistency must not be significantly worse than that for the original cluster,  $\Delta\chi^2 = (\chi')^2 - \chi^2$  < `EnergyDeltaChi2ForCrudeMerging` [1.0], where  $\chi = (E_C - p)/\sigma_{E_C}$ .

- (viii) Cone-base merging: Starting from the identified hadronic interaction point of each charged cluster, a cone of half-angle `CosineConeAngle` [0.9] is defined in the direction of the track-like segment of the cluster. Neutral clusters deeper in the calorimeter with more than 50% of the energy of lying within this cone may be merged providing the above  $\chi^2$  consistency requirements are satisfied. If there is no track-like segment at the start of the charged cluster, the track direction is used.
- (ix) Photon recovery: In dense jets minimum ionising particles may pass through the EM shower from a photon, resulting in a single reconstructed cluster. Cases where the hadron interacts a significant distance after the end of the EM shower are identified and photons overlapping with charged clusters are recovered.

#### 4.5. Re-clustering

The previous four stages of the PandoraPFA algorithm are found to perform well for jets with energy less than about 50 GeV. At higher energies the jet energy resolution degrades due to the increasing overlap between the hadronic showers from different particles. It is possible to detect such reconstruction failures by comparing the charged cluster energy,  $E_C$ , with the momentum of the associated track,  $p$ . A possible reconstruction failure is identified if  $|(E_C - p)/\sigma_{E_C}| > \text{ChiToAttemptReclustering}$  [3.0]. In this case the PandoraPFA algorithm attempts to find a more self-consistent clustering of the calorimeter hits. If, for example, a 10 GeV track is associated with a 20 GeV calorimeter cluster, shown schematically in Figure 5a), a potential reconstruction failure is identified. One possible approach would be to simply remove hits from the cluster until the cluster energy matched the track momentum. However, this does not use the full information in the event. Instead, the clustering algorithm is modified iteratively with the hope that a more correct clustering of the hits will be found. This is implemented by passing the hits in the cluster and the associated track(s) to the main clustering algorithm described in Sections 4.3 and 4.4. The algorithm is applied repeatedly, using successively smaller values of the parameters  $A$  and  $b$ , with the aim of splitting the original cluster so that the track momentum and associated cluster energy are compatible, as indicated in Figure 5a). In principle, completely different clustering algorithms could be tried. In cases where no significant improvement in the  $\chi^2$  compatibility of the track and associated cluster is found, the original cluster is retained.

In steps vii) and viii) of the topological clustering, described in Section 4.4, the case where too little energy is associated with the track is addressed. However, in a dense jet environment, the neutral cluster which should be associated with a charged cluster may itself be merged with another neutral cluster, as indicated in Figure 5b). In such cases the reclustering procedure acts on the combination of hits in the charged cluster associated to the track and nearby neutral clusters.

#### 4.6. Photon Identification and Recovery

A relatively sophisticated photon identification algorithm is applied to the reconstructed clusters. The longitudinal profile of the energy deposition,  $\Delta E_{obs}$ , as a function of number of radiation lengths from the shower start,  $t$ , is compared to that expected [24] for an EM shower:

$$\Delta E_{EM} \approx E_0 \frac{(t/2)^{a-1} e^{-t/2}}{\Gamma(a)} t,$$

$$\text{where } a = 1.25 + \frac{1}{2} \ln \frac{E_0}{E_c},$$

$E_0$  is the shower energy and  $E_c$  is the critical energy, which is chosen to give the appropriate average MC shower profile in the ECAL. The level of agreement is parameterised by the sum over samplings in radiation length of the fractional deviation of the cluster profile compared the expectation for an EM shower:

$$\delta = \frac{1}{E_0} \sum_i |\Delta E_{obs}^i - \Delta E_{EM}^i|.$$

This approach was preferred to a  $\chi^2$ -based metric as it is less sensitive to large local deviations which might arise from energy deposits from other nearby particles. The quantity  $\delta$  is minimised as a function of the assumed starting point of the shower,  $t_0$ . Hence the output of the shower shape algorithm is a measure of the consistency with the expected EM shower profile,  $\delta$ , and the starting depth of the shower in the ECAL,  $t_0$  (in radiation lengths). These variables are used as the basis for identifying clusters as photons. Transverse information is not used as this would make the photon identification algorithm more sensitive to over-lapping EM showers from very close photons.

#### 4.6.1. Photon Recovery

The compact nature of EM showers is utilised in an attempt to identify photons which may have been merged into the cluster associated with a hadronic shower. The transverse energy distribution (ECAL only) of the reconstructed clusters is determined assuming that the cluster originates from the IP. A peak finding algorithm attempts to identify localised energy depositions which are displaced from the associated track. If the longitudinal energy profile in these regions is consistent with being an EM shower, the relevant hits are removed from the cluster and used to form a new cluster (assumed to be a photon). Cases where removing the candidate photon would result in the remaining cluster energy being inconsistent with the associated track momentum are vetoed.

#### 4.7. Fragment Removal

At this late stage in PandoraPFA there are still a significant number of “neutral clusters” (not identified as photons) which are *fragments* of charged particle hadronic showers. An attempt is made to identify these clusters and merge them with the appropriate parent charged cluster. All non-photon neutral clusters,  $i$ , are compared to all charged clusters,  $j$ . For each pair of clusters a quantity,  $e_{ij}$ , is defined which encapsulates the evidence that cluster  $i$  is a fragment from cluster  $j$  using the following information: the number of calorimeter layers in which the minimum distance between the hits in the two clusters are separated by less than `FragmentRemovalContactCut` [2] pixels; the fractions of the energy of cluster  $i$  within three narrow cones defined by the first hadronic interaction in cluster  $j$ ; the minimum distance of the centroid within a layer of cluster  $i$  to the fitted helix describing the track associated to cluster  $j$ ; and the minimum distance between any of the hits in the two clusters. The requirement,  $R_{ij}$ , for the clusters to be merged, *i.e.* the cut on  $e_{ij}$ , depends on the location of the depth of the neutral cluster in the calorimeter and the change in the  $\chi^2$  for the track–cluster energy consistency that would occur if the clusters were merged,

$$\Delta\chi^2 = (p - E_j)^2 / \sigma_{E_j}^2 - (p - E_j - E_i)^2 / \sigma_{E_i}^2.$$

If  $e_{ij} > R_{ij}$  the clusters are merged. This *ad hoc* procedure gives extra weight to cases where the consistency of the track momentum and associated cluster energy improves as a result of merging the neutral cluster with the charged cluster.

#### 4.8. Formation of Particle Flow Objects

The final stage of PandoraPFA is to create Particle Flow Objects (PFOs) from the results of the clustering. Tracks are matched to clusters on the basis of the distance closest approach of the track projection into the first 10 layers of the calorimeter. If a hit is found within a distance `TrackClusterAssociationDistance` [10 mm] of the track extrapolation, an association is made. If an identified kink is consistent with being from a  $K^\pm \rightarrow \mu^\pm \nu$  or  $\pi^\pm \rightarrow \mu^\pm \nu$  decay the parent track is used to form the PFO, otherwise the daughter track is used. Relatively primitive particle identification is applied and the reconstructed PFOs, including four-momenta, are written out in LCIO [17] format. Figure 6a) shows an example of a PandoraPFA reconstruction of a 100 GeV jet from a  $Z \rightarrow u\bar{u}$  decay at  $\sqrt{s} = 200$  GeV. The ability to track particles in the high granularity calorimeter in the ILD detector concept can be seen clearly.

### 5. Parameterising Particle Flow Performance: $\text{rms}_{90}$

Figure 7 shows the distribution of PFA reconstructed energy for simulated  $(Z/\gamma)^* \rightarrow q\bar{q}$  events (light quarks only, *i.e.*  $q=u,d,s$ ) generated at  $\sqrt{s} = 200$  GeV with the Z decaying at rest, termed “Z  $\rightarrow$  uds” events. A cut on the polar angle of the generated  $q\bar{q}$  system,  $\theta_{q\bar{q}}$ , is chosen to avoid the barrel/endcap overlap region,  $|\cos \theta_{q\bar{q}}| < 0.7$ . Only light quark decays are considered as, currently, PandoraPFA does not include specific reconstruction algorithms to attempt to recover missing energy from semi-leptonic decays of heavy quarks. The reconstructed energy distribution of Figure 7 is not Gaussian. This is not surprising; one might expect a Gaussian core for perfectly reconstructed events, and tails corresponding to the population of events where confusion is significant. Quoting the rms, in this case 5.8 GeV, as a measure of the jet energy resolution over-emphasises the importance of these tails. In this paper, performance is quoted in terms of  $\text{rms}_{90}$ , which is defined as the rms in the smallest range of reconstructed energy which contains 90% of the events. For the data shown in Figure 7,  $\text{rms}_{90} = 4.1$  GeV (equivalent to a single jet energy resolution of 2.9%). The advantage of using  $\text{rms}_{90}$  is that it is robust and is relatively insensitive to the tails of the distribution; it parameterises the resolution for the bulk of the data. One possible criticism of this performance measure is that for a true Gaussian distribution,  $\text{rms}_{90}$  would be 21% smaller than the true rms. However, for the non-Gaussian distribution from PFlow reconstruction, this is not a fair comparison. For example, the central region of the reconstructed energy distribution<sup>3</sup> is 15% narrower than the equivalent Gaussian of  $\sigma = \text{rms}_{90}$  as shown in Figure 7. To determine the equivalent Gaussian statistical power, a MC study was performed assuming a signal with the shape of the PFA reconstructed energy distribution centred on  $x$  and a flat background. A fit to determine the value of  $x$  was performed using the shape of the PFA distribution as a resolution function (fitting template). The process was repeated assuming a signal with same number of events but now with a Gaussian energy distribution. The width of the Gaussian (for both the signal and the fitting function) was chosen to give the same statistical precision on  $x$  as obtained with the PFA resolution function. From a fit to signal and background components the same fitted uncertainty,  $\sigma_x$ , is obtained for a Gaussian with standard deviation of  $1.1 \times \text{rms}_{90}$ . On this basis it is concluded that the statistical power for PFlow reconstruction with PandoraPFA yielding  $\text{rms}_{90}$  is equivalent to a Gaussian resolution with  $\sigma = 1.1 \times \text{rms}_{90}$ . This conclusion does not depend strongly on the assumed relative normalisation of the signal and background or the total energy of the generated events.

<sup>3</sup>Here the best fit Gaussian to the region 196 – 205 GeV has an rms of 3.5 GeV

## 6. Particle Flow Performance

The performance of the PandoraPFA algorithm with the ILD detector concept is studied using MC samples of approximately 10000  $Z \rightarrow uds$  generated with the  $Z$  decaying at rest with  $E_Z = 91.2, 200, 360, \text{ and } 500 \text{ GeV}$ . These jet energies are typical of those expected at the ILC operating at  $\sqrt{s} = 0.5 - 1.0 \text{ TeV}$ . In addition, to study the performance at higher energies, events were generated with  $E_Z = 750 \text{ GeV}$  and  $1 \text{ TeV}$ . Jet fragmentation and hadronisation was performed using the PYTHIA [25] program tuned to the fragmentation data from the OPAL experiment [26]. The events were passed through the MOKKA simulation of the ILD detector concept which is described in detail in [12]. The LCPHYS[27] Geant4 physics list was used for the modelling of hadronic showers. For each set of events, the total energy is reconstructed and the jet energy resolution is obtained by dividing the total energy resolution by  $\sqrt{2}$ . Figure 8 shows the jet energy resolution as a function of the polar angle of the quarks in  $Z \rightarrow q\bar{q}$  events. The energy resolution does not vary significantly in the region  $|\cos \theta| < 0.975$ . A small degradation in the energy resolution is seen for the barrel-endcap overlap region,  $0.7 < |\cos \theta| < 0.8$ . In addition, there is a small degradation in performance at  $\cos \theta \approx 0$  due to the TPC central membrane and gaps between sections of the HCAL as simulated in the ILD detector model.

Jet Energy	rms	rms <sub>90</sub> ( $E_{jj}$ )	rms <sub>90</sub> ( $E_{jj}$ )/ $\sqrt{E_{jj}}$	rms <sub>90</sub> ( $E_j$ )/ $E_j$
45 GeV	3.4 GeV	2.4 GeV	25.2 %	(3.74 ± 0.05) %
100 GeV	5.8 GeV	4.1 GeV	29.2 %	(2.92 ± 0.04) %
180 GeV	11.6 GeV	7.6 GeV	40.3 %	(3.00 ± 0.04) %
250 GeV	16.4 GeV	11.0 GeV	49.3 %	(3.11 ± 0.05) %
375 GeV	29.1 GeV	19.2 GeV	81.4 %	(3.64 ± 0.05) %
500 GeV	43.3 GeV	28.6 GeV	91.6 %	(4.09 ± 0.07) %

Table 3: Jet energy resolution for  $Z \rightarrow uds$  events with  $|\cos \theta_{q\bar{q}}| < 0.7$ , expressed as: i) the rms of the reconstructed di-jet energy distribution,  $E_{jj}$ ; ii) rms<sub>90</sub> for  $E_{jj}$ ; iii) the effective constant  $\alpha$  in  $\text{rms}_{90}(E_{jj})/E_{jj} = \alpha(E_{jj})/\sqrt{E_{jj}(\text{GeV})}$ ; and iv) the fractional jet energy resolution for a single jet where  $\text{rms}_{90}(E_j) = \text{rms}_{90}(E_{jj})/\sqrt{2}$ .

Table 3 summarises the current performance of the PandoraPFA algorithm applied to ILD detector simulation. For the typical ILC jet energy range, 45 – 250 GeV, the energy resolution is significantly better than the best resolution achieved at LEP,  $\sigma_E/E \approx 0.65/\sqrt{E(\text{GeV})}$ . Table 3 also lists the single jet energy resolution. For jet energies in the range 45 – 375 GeV this is better than 3.8 %, which is necessary to resolve hadronic decays of  $W$  and  $Z$  bosons. These results clearly demonstrate the potential of PFlow calorimetry at the ILC; the jet energy resolution obtained is approximately a factor two better than might be achievable with a traditional calorimetric approach. Furthermore, it is expected that the performance of PandoraPFA will improve with future refinements to the algorithm.

It is worth noting, that for perfect PFlow reconstruction, the energy resolution would be described by  $\sigma_E/E \approx \alpha/\sqrt{E(\text{GeV})}$ , where  $\alpha$  is a constant. The fact that this does not apply is not surprising; as the particle density increases it becomes harder to correctly associate the calorimetric energy deposits to the particles and the confusion term increases. Also it should be noted that in a physics analysis involving multi-jet final states, the resolution may be degraded by imperfect jet finding.

## 7. Understanding Particle Flow Performance

PandoraPFA is a fairly complex algorithm, consisting of over 10,000 lines of C++. It has a number of distinct stages which interact with each other in the sense that reconstruction failures in one part of the software can be corrected at a later stage. The relative importance of the different stages in the reconstruction is investigated by turning off parts of the PandoraPFA algorithm. Table 4 compares the full PandoraPFA reconstruction with the algorithm run: a) without the topological cluster merging phase; b) without the reclustering phase; c) without running the photon clustering stage prior to the running the full clustering; d) without fragment removal; and e) the case where tracks from  $V^0$ s and kinks are not used in the event reconstruction. There are a number of notable features. The topological clustering and fragment removal algorithms are important at all energies. For low energy jets, the reclustering stage is not particularly important. This is because the primary clustering and topological clustering algorithms are sufficient in the relatively low particle density environment. With increasing jet energy, the reclustering stage becomes more important. For high energy jets ( $E > 100$  GeV) it is the single most important step in the reconstruction after the initial clustering. Running the dedicated photon clustering stage before the main clustering algorithm is advantageous for higher energy jets. The  $V^0$ /kink finding does not significantly improve the resolution, although it is an important part in the identification of the final reconstructed particles.

Algorithm	Jet Energy Resolution $\text{rms}_{90}(E_j)/E_j$ [%]			
	$E_j=45$ GeV	$E_j=100$ GeV	$E_j=180$ GeV	$E_j=250$ GeV
Full PandoraPFA	$3.74 \pm 0.05$	$2.92 \pm 0.04$	$3.00 \pm 0.04$	$3.11 \pm 0.05$
a) No Topological Clustering	$4.02 \pm 0.05$	$3.25 \pm 0.04$	$3.52 \pm 0.05$	$3.67 \pm 0.06$
b) No Reclustering	$3.83 \pm 0.05$	$3.30 \pm 0.04$	$3.91 \pm 0.05$	$4.19 \pm 0.07$
c) No Photon Clustering Stage	$3.66 \pm 0.05$	$2.99 \pm 0.04$	$3.13 \pm 0.04$	$3.31 \pm 0.05$
d) No Fragment Removal	$4.05 \pm 0.05$	$3.21 \pm 0.04$	$3.25 \pm 0.04$	$3.40 \pm 0.06$
e) No $V^0$ /Kink Tracks	$3.78 \pm 0.05$	$2.96 \pm 0.04$	$3.02 \pm 0.04$	$3.13 \pm 0.05$

Table 4: Jet energy resolutions ( $\text{rms}_{90}/E$ ) for the full PandoraPFA reconstruction compared to that obtained: a) without the topological cluster merging phase; b) without the reclustering phase; c) without running the photon clustering stage prior to the running the full clustering; d) without fragment removal; and e) the case where tracks from  $V^0$ s and kinks are not used in the event reconstruction.

The contributions to the jet energy resolution have been estimated by replacing different steps in PandoraPFA with algorithms which use MC information to perform: a) perfect reconstruction of photons as the first phase of the algorithm; b) perfect reconstruction of neutral hadrons; and c) perfect identification of fragments from charged hadrons. The jet energy resolutions obtained using these “perfect” algorithms enable the contributions from *confusion* to be estimated. In addition, studies using a deep HCAL enable the contribution from leakage to be estimated. Finally, MC information can be used to perform ideal track pattern recognition enabling the impact of imperfect track finding code to be assessed. Table 5 lists the estimated breakdown of the total jet energy into its components, including the contributions from calorimetric energy resolution (*i.e.* the energy resolution for photons and neutral hadrons). For the current PandoraPFA algorithm, the contribution from the calorimetric energy resolution,  $\approx 21\% / \sqrt{E}$ , dominates the jet energy resolution for 45 GeV jets. For higher energy jets, the confusion term dominates. This behaviour is summarised in Figure 9. The contributions from resolution and confusion are roughly equal for



120 GeV jets. From Table 5 it can be seen that the most important contribution for high energy jets is confusion due to neutral hadrons being lost within charged hadron showers. For all jet energies considered, fragments from charged hadrons, which tend to be relatively low in energy, do not contribute significantly to the jet energy resolution.

Contribution	Jet Energy Resolution $\text{rms}_{90}(E_j)/E_j$			
	$E_j=45$ GeV	$E_j=100$ GeV	$E_j=180$ GeV	$E_j=250$ GeV
Total	3.7 %	2.9 %	3.0 %	3.1 %
Resolution	3.0 %	2.0 %	1.6 %	1.3 %
Tracking	1.2 %	0.7 %	0.8 %	0.8 %
Leakage	0.1 %	0.5 %	0.8 %	1.0 %
Other	0.6 %	0.5 %	0.9 %	1.0 %
Confusion	1.7 %	1.8 %	2.1 %	2.3 %
i) Confusion (photons)	0.8 %	1.0 %	1.1 %	1.3 %
ii) Confusion (neutral hadrons)	0.9 %	1.3 %	1.7 %	1.8 %
iii) Confusion (charged hadrons)	1.2 %	0.7 %	0.5 %	0.2 %

Table 5: The PFlow jet energy resolution obtained with PandoraPFA broken down into contributions from: intrinsic calorimeter resolution, imperfect tracking, leakage and confusion. The different confusion terms correspond to: i) hits from photons which are lost in charged hadrons; ii) hits from neutral hadrons that are lost in charged hadron clusters; and iii) hits from charged hadrons that are reconstructed as a neutral hadron cluster.

The numbers in Table 5 can be used to obtain an semi-empirical parameterisation of the jet energy resolution:

$$\frac{\text{rms}_{90}}{E} = \frac{21}{\sqrt{E}} \oplus 0.7 \oplus 0.004E \oplus 2.1 \left( \frac{E}{100} \right)^{0.3} \%,$$

where  $E$  is the jet energy in GeV. The four terms in the expression respectively represent: the intrinsic calorimetric resolution; imperfect tracking; leakage and confusion. This functional form is shown in Figure 10. It is worth noting that the predicted jet energy resolutions for 375 GeV and 500 GeV jets are in good agreement with those found for MC events (see Table 3); these data were not used in the determination of the parameterisation of the jet energy resolution.

The ILC jet energy goal of  $\sigma_E/E < 3.8\%$  is reached in the jet energy range 40 GeV – 420 GeV. Figure 10 also shows a parameterisation of the jet energy resolution ( $\text{rms}_{90}$ ) obtained from a simple sum of the total calorimetric energy deposited in the ILD detector concept. It is worth noting that even for the highest energies jets considered, PFlow reconstruction significantly improves the resolution. The performance of PFlow calorimetry is compared to  $60\% / \sqrt{E(\text{GeV})} \oplus 2.0\%$  which is intended to give an *indication* of the resolution which might be achieved using a traditional calorimetric approach. For a significant range of the jet energies relevant for the ILC, PFlow results in a jet energy resolution which is roughly a factor two better than the best at LEP.

## 8. Dependence on Hadron Shower Modelling

The results of the above studies rely on the accuracy of the MC simulation in describing EM and hadronic showers. The Geant4 MC provides a good description of EM showers as has been demonstrated in a series of test-beam experiments [28] using a Silicon-Tungsten ECAL of

the type assumed for the ILD detector model. However, the uncertainties in the development of hadronic showers are much larger [29]. There are a number of possible effects which could affect PFlow performance: the hadronic energy resolution; the transverse development of hadronic showers which will affect the performance for higher energy jets where confusion is important; and the longitudinal development of the shower which will affect both the separation of hadronic and EM showers and the amount of leakage through the rear of the HCAL.

To assess the sensitivity of PFlow reconstruction to hadronic shower modelling uncertainties, five Geant4 physics lists are compared:

- QGSP\_BERT, Quark-Gluon String model[30] with the addition of the Precompound model of nuclear evaporation[31] (QGSP) for high energy interactions, and the Bertini (BERT) cascade model[32] for intermediate energy interactions;
- QGS\_BIC, Quark-Gluon String (QGS) for high energy interactions and the Binary cascade (BIC) model[33] for intermediate and low energies;
- FTFP\_BERT, the Fritiof (FTF) string-based model[34] with Precompound[31] for high energy interactions and the Bertini cascade model for intermediate energies;
- LHEP, based on the Low and High Energy Parameterised modes (LEP and HEP) of the GHEISHA package[35] used in Geant3;
- LCPhys[27], which uses a combination of the QGSP, LEP and BERT models.

These physics lists represent a wide range of models and result in significantly different predictions for total energy deposition, and the longitudinal and transverse shower profiles. For each Physics list, the calibration constants in PandoraPFA are re-tuned, but no attempt to re-optimize the algorithm is made. The jet energy resolutions obtained are given in Table 6. Whilst non-statistical differences are seen, the rms variations are relatively small, less than 4.2%. Whilst this might seem surprising, it should be noted that the effect on the jet energy resolution of the hadronic modelling is likely to be predominantly from the neutral hadron confusion term. This tends to dilute the sensitivity to the modelling of hadronic showers. For example, from Table 4 it can be seen that if the neutral hadron confusion term for 250 GeV jets is increased by 25%, when added in quadrature to the other terms, the overall jet energy resolution would only increase by 10%.

Physics List	Jet Energy Resolution $r = \text{rms}_{90}(E_j)/E_j$			
	45 GeV	100 GeV	180 GeV	250 GeV
LCPhys	$(3.74 \pm 0.05) \%$	$(2.92 \pm 0.04) \%$	$(3.00 \pm 0.04) \%$	$(3.11 \pm 0.05) \%$
QGSP_BERT	$(3.52 \pm 0.06) \%$	$(2.95 \pm 0.06) \%$	$(2.98 \pm 0.06) \%$	$(3.25 \pm 0.07) \%$
QGS_BIC	$(3.51 \pm 0.06) \%$	$(2.89 \pm 0.05) \%$	$(3.12 \pm 0.07) \%$	$(3.20 \pm 0.07) \%$
FTFP_BERT	$(3.68 \pm 0.08) \%$	$(3.10 \pm 0.06) \%$	$(3.24 \pm 0.06) \%$	$(3.26 \pm 0.08) \%$
LHEP	$(3.87 \pm 0.07) \%$	$(3.15 \pm 0.06) \%$	$(3.16 \pm 0.06) \%$	$(3.08 \pm 0.06) \%$
$\chi^2$ (4 d.o.f)	23.3	17.8	16.0	6.3
rms/mean ( $\sigma_r/\bar{r}$ )	4.2 %	3.9 %	3.5 %	2.5 %

Table 6: Comparison of the jet energy resolution obtained using different hadronic shower physics lists. The  $\chi^2$  consistency of the different models for each jet energy are given as are the rms variations between the five models.

From the above study it is concluded that, for 45 – 250 GeV jets, the jet energy resolution obtained from PFlow calorimetry as implemented in PandoraPFA does not depend strongly on the hadronic shower model; the observed differences are less than 5 %. This is an important statement; it argues strongly against the need for a test beam based demonstration of PFlow calorimetry (the design of such an experiment would be challenging). From test beam data the performance of the ECAL and HCAL systems can be demonstrated using single particles and the MC can be validated. Once the single particle performance is demonstrated, the uncertainties in extrapolating to the full PFlow performance for jets, which arise from the detailed modelling of hadronic showers, are likely to be less than 5 %.

## 9. Detector Design for Particle Flow Calorimetry

PFlow calorimetry requires the full reconstruction of the individual particles from the interaction. The optimisation of a detector designed for PFlow calorimetry extends beyond the calorimeters as tracking information plays a major role. This section presents a study of the general features of a detector designed for high granularity PFlow reconstruction.

### 9.1. General Arguments

PFlow calorimetry requires the efficient separation of showers from charged hadrons, photons and neutral hadrons. This implies high granularity calorimeters with both the ECAL and HCAL inside the detector solenoid. For high energy jets, failures in the ability to efficiently separate energy deposits from different particles, the *confusion* term, will dominate the jet energy resolution. The physical separation of calorimetric energy deposits from different particles will be greater in a large detector, scaling as the inner radius of the ECAL,  $R$ , in the barrel region and the detector length,  $L$ , in the endcap region. There are also arguments favouring a high magnetic field, as this will tend to deflect charged particles away from the core of a jet. The scaling law here is less clear. The separation between a charged particle and an *initially collinear* neutral particle will scale as  $BR^2$ . However, there is no reason to believe that this will hold on average for a jet of non-collinear neutral and charged particles. The true dependence of PFlow performance on the global detector parameters,  $B$  and  $R$  has to be evaluated empirically.

### 9.2. Particle Flow Optimisation Methodology

The dependence of the PFlow performance on the main detector parameters has been investigated using PandoraPFA. The studies are based on full reconstruction of the tracking and the calorimetric information. The results presented here use the Geant4 simulation of the LDC detector concept [11] which, from the point of view of PFlow, is essentially the same as the ILD detector concept described in Section 2. The starting point for the optimisation studies is the LD-CPrime detector model with a 3.5 T magnetic field, an ECAL inner radius of 1820 mm and a 48 layer ( $6\lambda_r$ ) HCAL. The ECAL and HCAL transverse segmentations are  $5 \times 5 \text{ mm}^2$  and  $3 \times 3 \text{ cm}^2$  respectively. The jet resolution is investigated as a function of a number of parameters.

### 9.3. HCAL Depth

For good PFlow performance both the ECAL and HCAL need to be within the detector solenoid. Consequently, in addition to the cost of the HCAL, the HCAL thickness impacts the cost of the overall detector through the radius of the superconducting solenoid. The thickness of

the HCAL determines the average fraction of the jet energy that is contained within the calorimeter system. The impact of the HCAL thickness on PFlow performance is assessed by changing the number of HCAL layers in the LDCPrime model from 32 to 63. This corresponds to a variation of  $4.0 - 7.9 \lambda_l$  in the HCAL ( $4.8 - 8.7 \lambda_l$  in the ECAL+HCAL combined).

The study of the optimal HCAL thickness depends on the possible use of the instrumented return yoke (the muon system) to correct for leakage of high energy showers out of the rear of the HCAL. The effectiveness of this approach is limited by the fact that, for much of the polar angle, the muon system is behind the relatively thick solenoid ( $2\lambda_l$  in the MOKKA simulation of the detector). Nevertheless, to assess the possible impact of using the muon detector as a “tail-catcher”, the energy depositions in the muon detectors were included in the PandoraPFA reconstruction. Whilst the treatment could be improved upon, it provides an indication of how much of the degradation in jet energy resolution due to leakage can be recovered in this way. The results are summarised in Figure 11 which shows the jet energy resolution obtained from PandoraPFA as a function of the HCAL thickness. The effect of leakage is clearly visible, with about half of the degradation in resolution being recovered when including the muon detector information. For jet energies of 100 GeV or less, leakage is not a major contributor to the jet energy resolution provided the HCAL is approximately  $4.7\lambda_l$  thick (38 layers). However, for 180 – 250 GeV jets this is not sufficient; for leakage not to contribute significantly to the jet energy resolution at  $\sqrt{s} = 1$  TeV, the results in Figure 11 suggest that the HCAL thickness should be between  $5.5 - 6.0\lambda_l$  for an ILC detector.

#### 9.4. Magnetic Field versus Detector Radius

The LDCPrime model assumes a magnetic field of 3.5 T and an ECAL inner radius of 1820 mm. A number of variations on these parameters were studied: i) variations in the ECAL inner radius from 1280 – 2020 mm with  $B = 3.5$  T; ii) variations the  $B$  from 2.5 – 4.5 T with  $R = 1825$  mm; and iii) variations of both  $B$  and  $R$ . In total thirteen sets of parameters were considered spanning a wide range of  $B$  and  $R$ . The parameters include those considered by the LDC, GLD [36], and SiD [37] detector concept groups for the ILC. In each case PFlow performance was evaluated for 45, 100, 180, and 500 GeV jets.

Figure 12 shows the dependence of the jet energy resolution as a function of: a) magnetic field (fixed  $R$ ) and b) ECAL inner radius (fixed  $B$ ). For 45 GeV jets, the dependence of the jet energy resolution on  $B$  and  $R$  is rather weak because, for these energies, it is the intrinsic calorimetric energy resolution rather than the confusion term that dominates. For higher energy jets, where the confusion term dominates the resolution, the jet energy resolution shows a stronger dependence on  $R$  than  $B$ .

The jet energy resolutions are reasonably well described by the function:

$$\frac{\text{rms}_{90}}{E} = \frac{21}{\sqrt{E}} \oplus 0.7 \oplus 0.004E \oplus 2.1 \left( \frac{R}{1825} \right)^{-1.0} \left( \frac{B}{3.5} \right)^{-0.3} \left( \frac{E}{100} \right)^{0.3} \%,$$

where  $E$  is measured in GeV,  $B$  in Tesla, and  $R$  in mm. This is the quadrature sum of four terms: i) the estimated contribution to the jet energy resolution from the intrinsic calorimetric resolution; ii) the contribution from track reconstruction; iii) the contribution from leakage; and iv) the contribution from the confusion term obtained empirically from a fit to the data of Figure 12 and several models where both  $B$  and  $R$  are varied [12]. In fitting the confusion term, a power-law

form,  $\kappa B^\alpha R^\beta E^\gamma$ , is assumed. This functional form provides a reasonable parameterisation of the data; the majority of the data points lie within  $2\sigma$  of the parameterisation.

From the perspective of the optimisation of a detector for PFlow, these studies show that for the PandoraPFA algorithm, the confusion term scales as approximately  $B^{0.3}R$ , *i.e.* for good PFlow performance a large detector radius is significantly more important than a very high magnetic field.

### 9.5. ECAL and HCAL Design

The dependence of PFlow performance on the transverse segmentation of the ECAL was studied using modified versions of the LDCPrime model. The jet energy resolution is determined for different ECAL Silicon pixel sizes;  $5 \times 5 \text{ mm}^2$ ,  $10 \times 10 \text{ mm}^2$ ,  $20 \times 20 \text{ mm}^2$ , and  $30 \times 30 \text{ mm}^2$ . The two main clustering parameters in the PandoraPFA algorithm were re-optimised for each ECAL granularity. The PFlow performance results are summarised in Figure 13a. For 45 GeV jets, the dependence is relatively weak since the confusion term is not the dominant contribution to the resolution. For higher energy jets, a significant degradation in performance is observed with increasing pixel size. Within the context of the current reconstruction, the ECAL transverse segmentations have to be at least as fine as  $10 \times 10 \text{ mm}^2$  to meet the ILC jet energy requirement of  $\sigma_E/E < 3.8\%$  for the jet energies relevant at  $\sqrt{s} = 1 \text{ TeV}$ , with  $5 \times 5 \text{ mm}^2$  being preferred.

A similar study was performed for the HCAL. The jet energy resolution obtained from PandoraPFA was investigated for HCAL scintillator tile sizes of  $1 \times 1 \text{ cm}^2$ ,  $3 \times 3 \text{ cm}^2$ ,  $5 \times 5 \text{ cm}^2$  and  $10 \times 10 \text{ cm}^2$ . The PFlow performance results are summarised in Figure 13b. From this study, it is concluded that the ILC jet energy resolution goals can be achieved an HCAL transverse segmentation of  $5 \times 5 \text{ cm}^2$ . For higher energy jets going to  $3 \times 3 \text{ cm}^2$  leads to a significant improvement in resolution. From this study there appears to be no significant motivation for  $1 \times 1 \text{ cm}^2$  granularity over  $3 \times 3 \text{ cm}^2$ . The results quoted here are for an analogue scintillator tile calorimeter. The conclusions for a digital, *e.g.* RPC-based, HCAL might be different.

### 9.6. Summary

Based on the above studies, the general features of a detector designed for high granularity PFlow calorimetry are:

- ECAL and HCAL should be inside the solenoid.
- The detector radius should be as large as possible, the confusion term scales approximately with the ECAL inner radius as  $R^{-1}$ .
- To fully exploit the potential of PFlow calorimetry the ECAL transverse segmentation should be at least as fine as  $5 \times 5 \text{ mm}^2$ .
- For the HCAL longitudinal segmentation considered here, there is little advantage in transverse segmentation finer than  $3 \times 3 \text{ cm}^2$ .
- The argument for a very high magnetic field is relatively weak as the confusion term scales as  $B^{-0.3}$ .

These studies, based on the PandoraPFA algorithm, motivated the design of the ILD detector concept for the ILC as is discussed in more detail in Chapter 2 of [12].

## 10. Particle Flow for Multi-TeV Colliders

In this section the potential of PFlow Calorimetry at a multi-TeV  $e^+e^-$  collider, such as CLIC [38], is considered. Before the results from the LHC are known it is difficult to fully define the jet energy requirements for a CLIC detector. However, if CLIC is built, it is likely that the construction will be phased with initial operation at ILC-like energies followed by high energy operation at  $\sqrt{s} \sim 3$  TeV. It has been shown in this paper that PFlow calorimetry is extremely powerful for ILC energies. Given that the confusion term increases with energy, it is not *a priori* clear that PFlow calorimetry is suitable for higher energies. This questions needs to be considered in the context of the possible physics measurements where jet energy resolution is likely to be important at  $\sqrt{s} \sim 3$  TeV. For example, the reconstruction of the jet energies in  $e^+e^- \rightarrow q\bar{q}$  events is unlikely to be interest. Assuming the main physics processes of interest consist of final states with between six and eight fermions, the likely relevant jet energies will be in the range 375 – 500 GeV. To study the potential of the PFlow calorimetry for these jet energies the ILD concept, which is optimised for ILC energies, was modified; the HCAL thickness was increased from  $6\lambda_I$  to  $8\lambda_I$  and the magnetic field was increased from 3.5 T to 4.0 T. The jet energy resolution obtained for jets from  $Z \rightarrow u\bar{u}, d\bar{d}, s\bar{s}$  decays at rest are listed in Table 7. For high energy jets, the effect of the increased HCAL thickness (the dominant effect) and increased magnetic field is significant. Despite the increased particle densities, the jet energy resolution ( $\text{rms}_{90}$ ) for 500 GeV jets obtained from PFlow is 3.5 %. This is equivalent to  $78\% / \sqrt{E(\text{GeV})}$ . This is likely to be *at least* competitive with a traditional calorimetric approach, particularly when the constant term in Equation 1 and the contribution from non-containment are accounted for. Furthermore, it should be remembered that PandoraPFA has not been optimised for such high energy jets and improvements can be expected. It is also worth noting that the purely calorimetric energy resolution ( $\text{rms}_{90}$ ) for 500 GeV jets with the modified ILD concept is equivalent to  $115\% / \sqrt{E(\text{GeV})}$  and, thus, the gain from PFlow reconstruction is still significant.

Jet Energy	$\text{rms}_{90}(E_{jj}) / \sqrt{E_{jj}}$		$\text{rms}_{90}(E_j) / E_j$	
	3.5 T & $6\lambda_I$	4 T & $8\lambda_I$	3.5 T & $6\lambda_I$	4 T & $8\lambda_I$
45 GeV	25.2 %	25.2 %	$(3.74 \pm 0.05)\%$	$(3.74 \pm 0.05)\%$
100 GeV	29.2 %	28.7 %	$(2.92 \pm 0.04)\%$	$(2.87 \pm 0.04)\%$
180 GeV	40.3 %	37.5 %	$(3.00 \pm 0.04)\%$	$(2.80 \pm 0.04)\%$
250 GeV	49.3 %	44.7 %	$(3.11 \pm 0.05)\%$	$(2.83 \pm 0.05)\%$
375 GeV	81.4 %	71.7 %	$(3.64 \pm 0.05)\%$	$(3.21 \pm 0.05)\%$
500 GeV	91.6 %	78.0 %	$(4.09 \pm 0.07)\%$	$(3.49 \pm 0.07)\%$

Table 7: Comparisons of jet energy resolutions for two sets of detector parameters. This jet energy resolution shown is for  $(Z/\gamma)^* \rightarrow uds$  events with  $|\cos\theta_{q\bar{q}}| < 0.7$ . It is expressed as: i) the effective constant  $\alpha$  in  $\text{rms}_{90}(E_{jj})/E_{jj} = \alpha(E_{jj})/\sqrt{E_{jj}(\text{GeV})}$ , where  $E_{jj}$  is the total reconstructed energy; and ii) the fractional jet energy resolution for a single jet where  $\text{rms}_{90}(E_j) = \text{rms}_{90}(E_{jj})/\sqrt{2}$ .

### 10.1. Gauge Boson Mass Reconstruction

A requirement for a detector at a future linear collider is the ability to separate hadronic W and Z decays. It was on this basis that the ILC jet energy resolution goal of  $\sigma_E/E \lesssim 3.8\%$  was justified. The performance of PFlow calorimetry has, up to this point, been considered in terms of the jet energy resolution from particles decaying at rest. This is reasonable since one of the

main goals of a future linear collider will be to study the physics Beyond the Standard Model (BSM) which hopefully will be uncovered at the LHC. Thus, many of the processes of interest are likely to be produced relatively close to threshold. In this case, the new particle(s) will be produced almost at rest. Similarly, for processes where a new particle is produced in association with one or more gauge bosons, the gauge bosons will be produced almost at rest. However, it is also possible that gauge bosons may be produced from the decays of BSM particles. In this case, the W/Z decays will not be at rest and the di-jet system will be boosted. At a multi-TeV lepton collider the boost may be significant as the energies of the gauge bosons are potentially in the range 500 GeV–1 TeV. For PFlow calorimetry there are a number of effects associated with highly boosted jets:

- The jet particle multiplicities are lower than those for jets of the same energy produced from decays at rest. This increases the average energy of the particles in the jet and, consequently, will result in less containment of the hadronic showers (greater leakage);
- The energies of the jets in the di-jet system will, in general, not be equal. Where one of the jets is much higher in energy than the other PFlow performance will tend to degrade.
- The high jet boost decreases the average separation of the particles in the jet. This will tend to increase the confusion term.
- The two jets from the decay of a highly boosted gauge boson will tend to overlap to form a “mono-jet”, as shown in Figure 14. The overlapping of jets has the potential to increase the confusion term.

Due to the likely increased confusion term, reconstructing the invariant mass of high energy gauge bosons presents a challenge for PFlow calorimetry. However, it should be noted that it may be even more challenging for a traditional calorimetric approach as it is now necessary to reconstruct the invariant mass of a single system of nearby particles which will not be well-resolved in the calorimeters.

The PFlow reconstruction of boosted gauge bosons has been investigated by generating MC samples of  $ZZ \rightarrow d\bar{d}\nu\bar{\nu}$  and  $W^+W^- \rightarrow u\bar{d}\mu^-\bar{\nu}_\mu$  events at  $\sqrt{s} = 0.25, 0.5, 1.0$  and  $2.0$  TeV. These final states give clean samples of single hadronic Z and W decays (the muons from the W decays are easy to identify and remove). The PFlow reconstructed W and Z invariant mass distributions are shown in Figure 15 and the corresponding mass resolutions are given in Table 8. A direct comparison with the jet energy resolutions of Table 7 is not straightforward due to the effects described above. However, the mass resolution ( $\text{rms}_{90}$ ) of 2.8 GeV obtained from decays of gauge bosons with  $E = 125$  GeV is compatible with that expected from the jet energy resolution of Table 7 after accounting for the gauge boson width.

For the ILC operating at  $\sqrt{s} = 0.5 - 1.0$  TeV, the typical energies of the gauge bosons of interest are likely to be in the range  $E_{W/Z} = 125 - 250$  GeV. Here the reconstructed W and Z mass peaks are well resolved. The statistical separation, which is quantified in Table 8, is approximately  $2.5\sigma$ , *i.e.* the separation between the two peaks is approximately 2.5 times greater the effective mass resolution.

For CLIC operating at  $\sqrt{s} = 3$  TeV, the relevant gauge boson energies are likely to be in the range  $0.5 - 1.0$  TeV. At the low end of this range there is reasonable separation ( $2.1\sigma$ ) between the W and Z peaks. Even for 1 TeV W/Z decays, where the events mostly appear as a single energetic mono-jet, the mass resolution achieved by the current version of PandoraPFA allows separation between W and Z decays at the  $1.5\sigma$  level. It should be remembered that PandoraPFA

$E_{W/Z}$	$\text{rms}_{90}(m)$	$\sigma_m/m$	W/Z sep	$\epsilon$
125 GeV	2.8 GeV	2.9 %	$2.7\sigma$	91 %
250 GeV	3.0 GeV	3.5 %	$2.5\sigma$	89 %
500 GeV	3.9 GeV	5.1 %	$2.1\sigma$	84 %
1000 GeV	6.4 GeV	7.0 %	$1.5\sigma$	78 %

Table 8: Invariant mass resolutions for the hadronic system in simulated  $ZZ \rightarrow d\bar{d}\nu\bar{\nu}$  and  $W^+W^- \rightarrow u\bar{d}\mu^-\bar{\nu}_\mu$  events in the ILD detector concept. The W/Z separation numbers, which take into account the tails, are defined such that a  $2\sigma$  separation means that the optimal cut in the invariant mass distribution results in 15.8 % of events being mis-identified. The equivalent W/Z identification efficiencies,  $\epsilon$ , are given in the final column. Even with infinitely good mass resolution, the best that can be achieved is 94 % due to the tails of the Breit-Wigner distribution and, thus, the possible range for  $\epsilon$  is 50 – 94 %;

has not been optimised for such high energy jets, and these results represent a lower bound on what can be achieved. From this result it is concluded that PFlow calorimetry is certainly not ruled out for a multi-TeV lepton collider.

## 11. Conclusions

A sophisticated particle flow reconstruction algorithm, PandoraPFA, has been developed to study the potential of high granularity Particle Flow calorimetry at a future linear collider. The algorithm incorporates a number of techniques, *e.g.* topological clustering and statistical reclustering, which take advantage of the highly segmented calorimeters being considered for the ILC and beyond.

PandoraPFA has been applied to the reconstruction of simulated events in the ILD detector concept for the ILC. The results presented in this paper provide the first conclusive demonstration that Particle Flow Calorimetry can meet the ILC requirements for jet energy resolution. For jets in the energy range 40–400 GeV, the jet energy resolution,  $\sigma_E/E$ , is better than 3.8 %. For the jet energies relevant at the ILC, the jet energy resolution is approximately a factor of two better than the best achieved at LEP. The conclusions do not depend strongly on the details of the modelling of hadronic showers.

PandoraPFA has been used to investigate the factors limiting the performance of Particle Flow calorimetry. For jet energies below approximately 100 GeV, the intrinsic calorimetric resolution dominates the jet energy resolution. For higher energy jets, the confusion term (*i.e.* imperfect reconstruction) dominates. The largest single contribution to the confusion term arises from the mis-assignment of energy from neutral hadrons.

PandoraPFA has been used to study design of a detector optimised for high granularity Particle Flow calorimetry demonstrating the importance of high transverse segmentation in the electromagnetic and hadron calorimeters. The confusion term, which dominates the jet energy resolution for high energy jets, scales as approximately  $B^{-0.3}R^{-1}$ , where  $B$  is the solenoidal magnetic field strength and  $R$  is the inner radius of the electromagnetic calorimeter.

In addition, PandoraPFA has been used to perform a preliminary study of the potential of Particle Flow calorimetry at a multi-TeV collider such as CLIC. For decays at rest, a jet energy resolution below 3.8 % is achievable for jets with energies less than approximately 600 GeV. Reasonable separation of the hadronic decays of W and Z bosons is achievable for W/Z energies of up to approximately 1 TeV.



In conclusion, the studies described in this paper provide the first proof of principle of Particle Flow calorimetry at a future lepton collider. For ILC energies,  $\sqrt{s} = 0.5 - 1.0$  TeV, unprecedented jet energy resolution can be achieved. Whilst the potential at a multi-TeV collider needs further investigation, the results presented in this paper are promising.

## 12. Acknowledgements

I would like to acknowledge: the UK Science and Technology Facilities Council (STFC) for the continued support of this work; my colleagues on the ILD detector concept for providing the high quality simulation and software frameworks used for these studies; Vasily Morgunov for many interesting and useful discussions on Particle Flow reconstruction; and David Ward for reading the near final draft of this paper.

## References

- [1] J.-C. Brient and H. Videau, “The calorimetry at a future  $e^+e^-$  linear collider”, arXiv:hep-ex/0202004v1 (2002).
- [2] International Linear Collider reference design report. 1: Executive summary. 2: Physics at the ILC. 3: Accelerator. 4: Detectors, J. Brau (ed.), *et al.*, ILC-REPORT-2007-001 (2007).
- [3] M. A. Thomson, Proc. of EPS-HEP 2003, Aachen. Topical Vol. of Eur. Phys. J. C Direct (2004).
- [4] I. G. Knowles and G. D. Lafferty, J. Phys. **G23** (1997) 731.
- [5] M. G. Green, S. L. Lloyd, P. N. Ratoff and D. R. Ward, “Electron-Positron Physics at the Z”, IoP Publishing (1998).
- [6] ALEPH Collaboration, D. Buskulic *et al.*, Nucl. Instr. and Meth. **A360** (1995) 481.
- [7] N. Akchurin, *et al.*, Nucl. Instr. and Meth. **A537** (2005) 29.
- [8] F. Gaede, Nucl. Instr. and Meth. **A559** (2006) 177.
- [9] P. de Freitas, *et al.*, <http://polzope.in2p3.fr:8081/MOKKA>.
- [10] GEANT4 collaboration, S. Agostinelli *et al.*, Nucl. Instr. and Meth. **A506** (2003) 3;  
GEANT4 collaboration, J. Allison *et al.*, IEEE Trans. Nucl. Sci. 53 (2006) 1.
- [11] Detector Outline Document for a Large Detector Concept, D. Kisieleska *et al.*, (2006).  
<http://www.ilclde.org/documents/dod/>
- [12] ILD Letter of Intent, <http://www.ilcild.org/>
- [13] V. L. Mogunov, “Energy-flow Method for Multi-jet Effective Mass Reconstruction in the Highly Granular TESLA Calorimeter”, proceedings of the Snowmass Summer Study on the Future of Particle Physics, Snowmass, U.S.A. (2001).
- [14] A. Raspereza, arXiv:physics/0601069 (2006).
- [15] M. Charles, arXiv:0901.4670v2 (2009).
- [16] J. C. Brient, *et al.*, “CALICE Report to the R&D Review Panel”, ILC-DET-2007-024 (2007); arXiv:0707.1245.
- [17] F. Gaede, T. Behnke, N. Graf, and T. Johnson, “LCIO: A persistency framework for linear collider simulation studies”, Proceedings of CHEP 03, La Jolla, California, March 2003; arXiv-physics:0306114 (2003),
- [18] T. Behnke, *et al.*, “Track Reconstruction for a Detector at TESLA”, LC-DET-2001-029 (2001), and references therein.
- [19] DELPHI Collaboration, DELPHI Data Analysis Program (DELANA) User’s Guide, DELPHI 89-44 PROG 137 (1989).
- [20] TESLA Technical Design Report, DESY 2001-011, ECFA 2001-2009 (2001).
- [21] A. Raspereza, “LDC Tracking Package”, Proceedings of LCWS2007, DESY, Hamburg, June 2007.
- [22] M. A. Thomson, “Progress with Particle Flow Calorimetry”, Proceedings of LCWS2007, DESY, Hamburg, June 2007. arXiv:0709.1360.
- [23] “GEAR - a geometry description toolkit for ILC reconstruction software”,  
[http://ilcsoft.desy.de/portal/software\\_packages/gear](http://ilcsoft.desy.de/portal/software_packages/gear)”.
- [24] Particle Data Group, Phys. Lett. **B667** (2008) 1.
- [25] T. Sjöstrand, Comp. Phys. Comm. **135** (2001) 238.
- [26] OPAL Collaboration, G. Alexander *et al.*, Z. Phys. **C69** (1996) 543.
- [27] “Linear Collider Physics List”,  
[http://www.slac.stanford.edu/comp/physics/geant/slac\\_physics\\_lists/ilc/ilc\\_physics\\_list.html](http://www.slac.stanford.edu/comp/physics/geant/slac_physics_lists/ilc/ilc_physics_list.html)

- [28] CALICE Collaboration, C. Adloff *et al.*, accepted for publication by NIMA (2009); arXiv:0811.2354.
- [29] R. Wigmans, Proc. of HSW06, Fermilab, 2006, AIP Conf. Proc. 896 (2007) 123.
- [30] G. Folger and J.-P. Wellisch, "String Parton Models in Geant4", CHEP03, La Jolla, California, March 2003, nucl-th/0306007;  
N. S. Amelin *et al.*, Phys. Rev. Lett. **67** (1991) 1523;  
L. V. Bravina *et al.*, Phys. Rev. Lett. **344** (1995) 49.
- [31] Geant4 Physics Reference Manual, Section IV, Chapter 28.
- [32] M. P. Guthrie, R. G. Alsmiller and H. W. Bertini, Nucl. Instr. and Meth. **A66** (1968) 29.
- [33] G. Folger, V. N. Ivanchenko and J.-P. Wellisch, Eur. Phys. J. **A21** (2004) 407.
- [34] B. Anderson, G. Gustafson and B. Nielsson-Almqvist, Nucl. Phys. **281** (1987) 289.
- [35] H. Fesefeld, "Simulation of hadronic showers, physics and applications", Technical Report PITHA 85-02, Aachen, Germany, September 1985.
- [36] GLD Concept Study, arXiv:physics/060071154v1 (2006).
- [37] SID Letter of Intent, <http://silicondetector.org/SiD/LOI>.
- [38] G. Guignard (ed.), *et al.*, "A 3 TeV Linear Collider Based on CLIC Technology", CERN-2000-008 (2000).

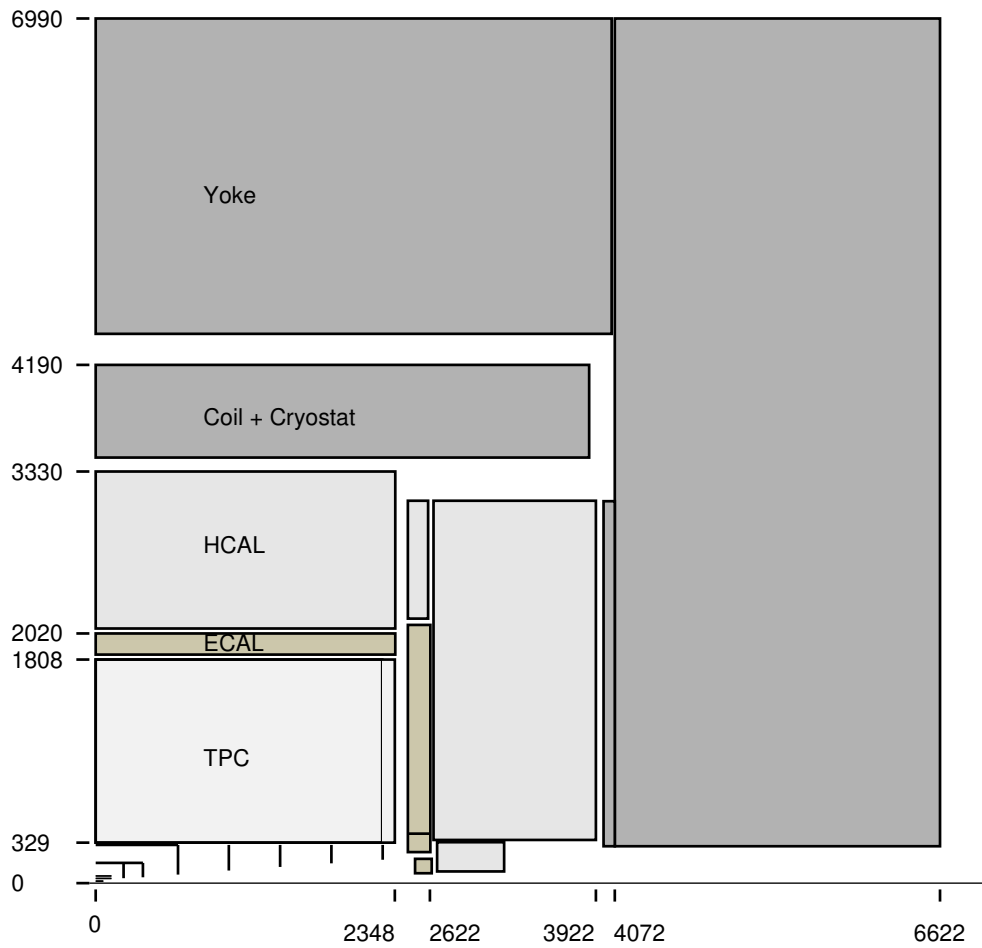


Figure 1: A quadrant of the ILD detector concept showing the main dimensions and layout of the sub-detector components.

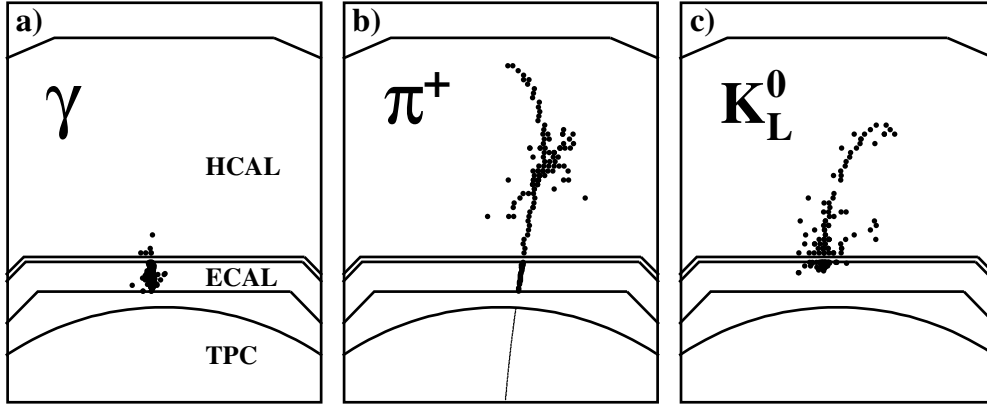


Figure 2: Example simulated single particle interactions in the ILD detector concept: a) a 10 GeV photon; b) a 10 GeV  $\pi^+$  and c) a 10 GeV  $K_L^0$ . Hits in the TPC, ECAL and HCAL are shown. For the ECAL (HCAL) all hits with energy depositions  $> 0.5$  ( $0.3$ ) minimum ionising particle equivalent are displayed. Simulated TPC hits are digitised assuming 227 radial rows of readout pads.

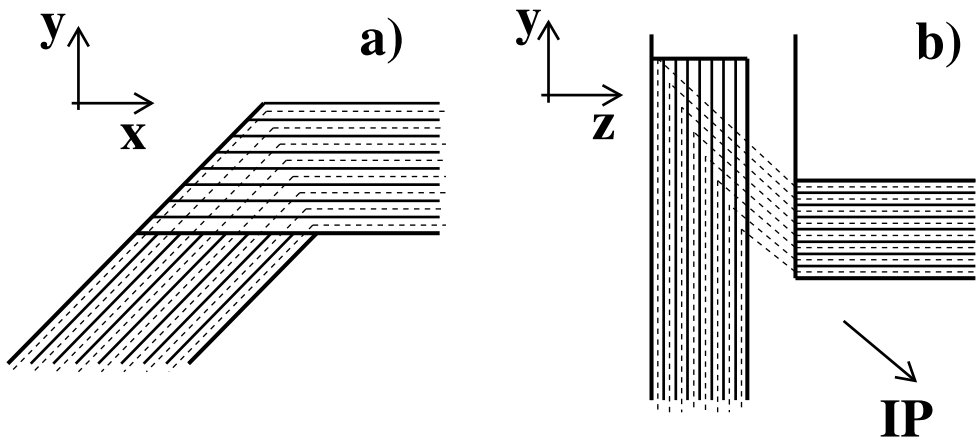


Figure 3: Schematic showing the definition of the pseudo-layer assignment for calorimeter hits. The solid lines indicate the positions of the physical ECAL layers and the dashed lines show the definition of the virtual pseudo-layers. a) The  $xy$ -view showing the CALICE stave structure for the ECAL. Here hits in the first layer of the stave can be deep in the overall calorimeter. b) The  $xz$ -view showing a possible layout for the ECAL barrel/endcap overlap region. Here the pseudo-layers are defined using the projection back to the IP such that the pseudo-layer is closely related to the depth in the calorimeter.

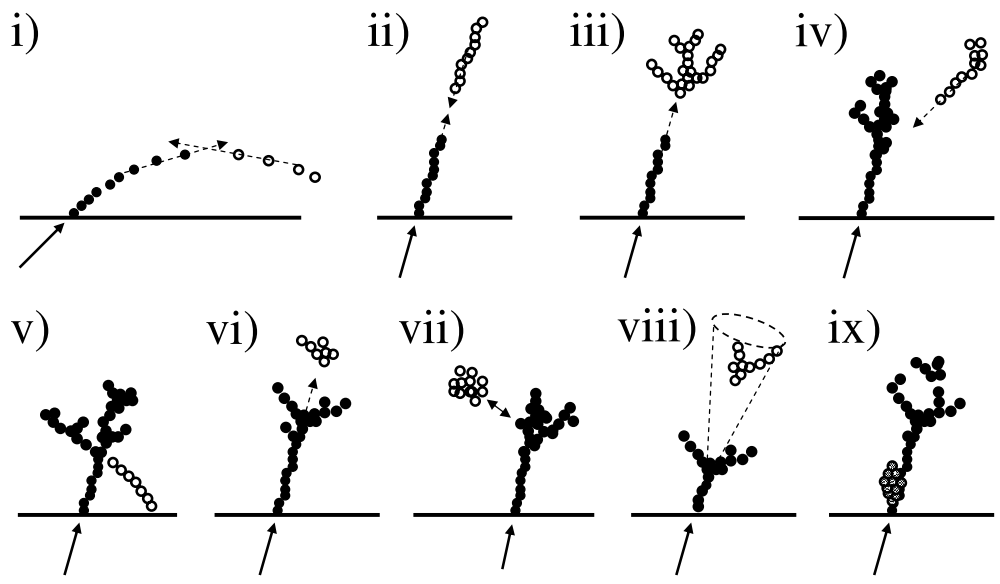


Figure 4: The main topological rules for cluster merging: i) looping track segments; ii) track segments with gaps; iii) track segments pointing to hadronic showers; iv) track-like neutral clusters pointing back to a hadronic shower; v) back-scattered tracks from hadronic showers; vi) neutral clusters which are close to a charged cluster; vii) a neutral cluster near to a charged cluster; viii) cone association; and ix) recovery of photons which overlap with a track segment. In each case the arrow indicates the track, the filled points represent the hits in the associated cluster and the open points represent the hits in the neutral cluster.

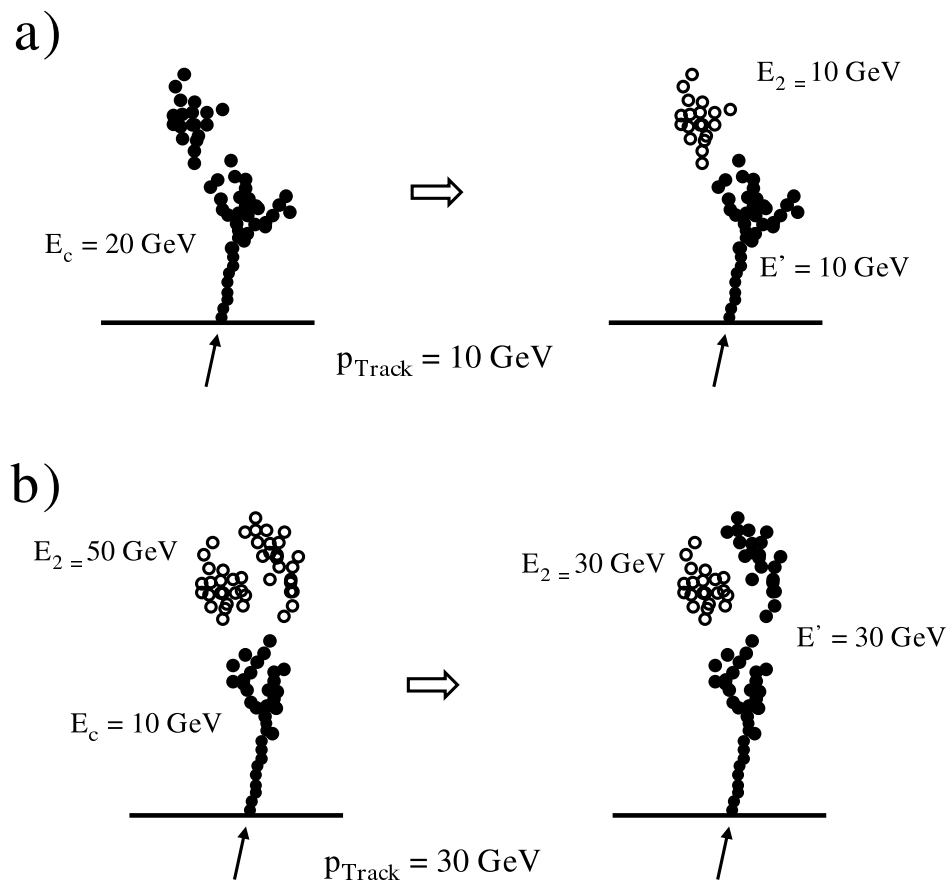


Figure 5: Schematic examples of the main reclustering strategies used in PandoraPFA. The arrows indicates the track, the filled points represent the hits in the associated charged cluster and the open points represent the hits in the neutral cluster. a) Here the charged cluster energy is initially significantly greater than the associated track momentum. The hits are reclustered using modified parameters for the clustering algorithm in the hope that a more consistent solution can be found. b) Here the cluster energy is significantly less than the associated track momentum. The topological association algorithms vii) and viii) have not added the neutral cluster as his would have resulted in a charged cluster with too much energy for the track momentum. The hits are reclustered in the hope that the neutral cluster naturally splits in such a way that the topological association algorithm will now make the correct association.

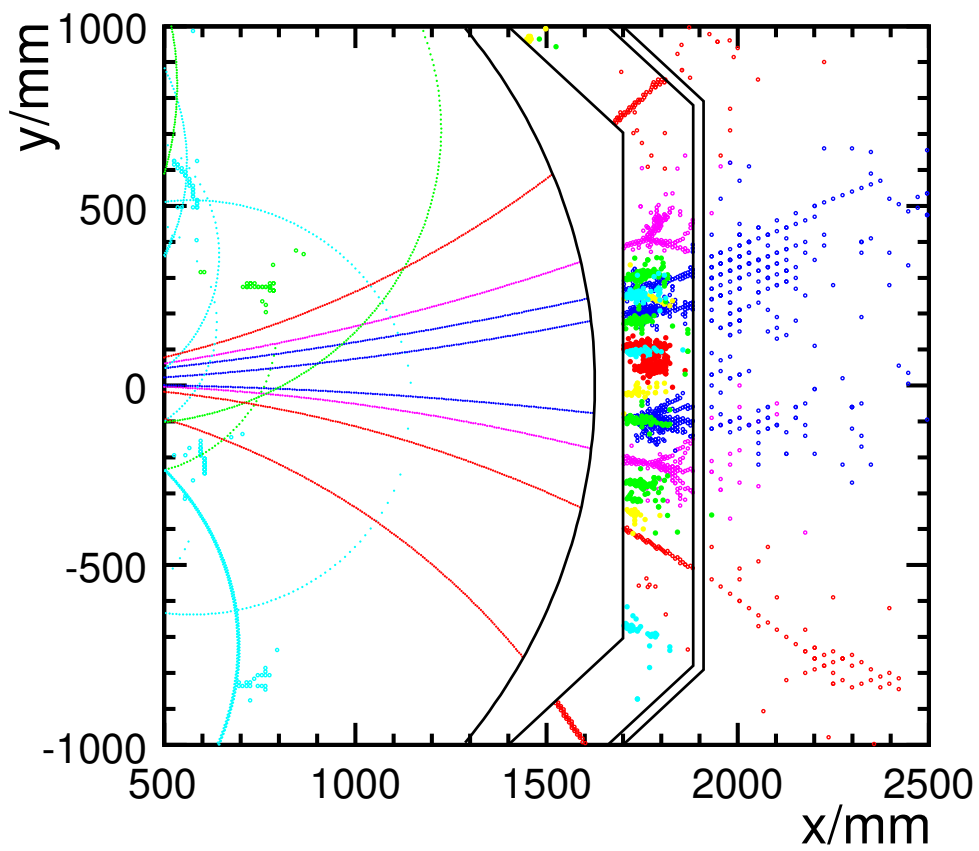


Figure 6: PandoraPFA reconstruction of a 100 GeV jet in the MOKKA simulation of the ILD detector. The different PFOs are shown by colour/grey-shade according to energy.

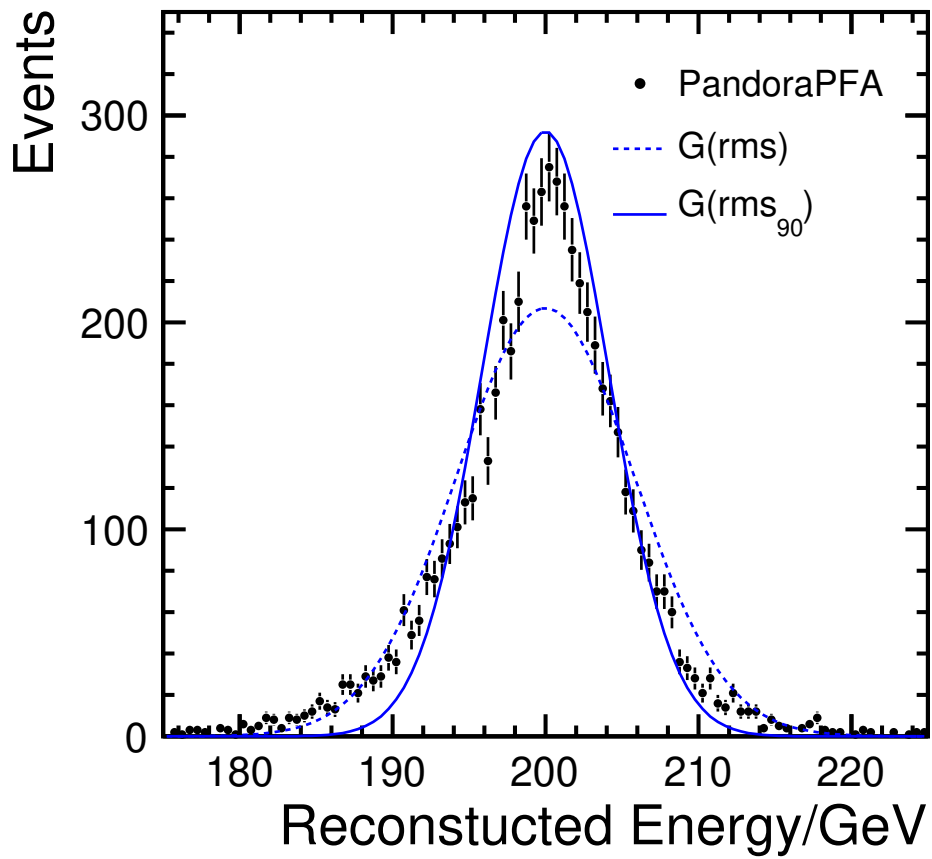


Figure 7: The total reconstructed energy from reconstructed PFOs in 200 GeV  $Z \rightarrow uds$  events for initial quark directions within the polar angle acceptance  $|\cos \theta_{q\bar{q}}| < 0.7$ . The dotted line shows the best fit Gaussian distribution with an rms of 5.8 GeV. The solid line shows a Gaussian distribution, normalised to the same number of events, with standard deviation equal to  $\text{rms}_{90}$  (*i.e.*  $\sigma = 4.1$  GeV).



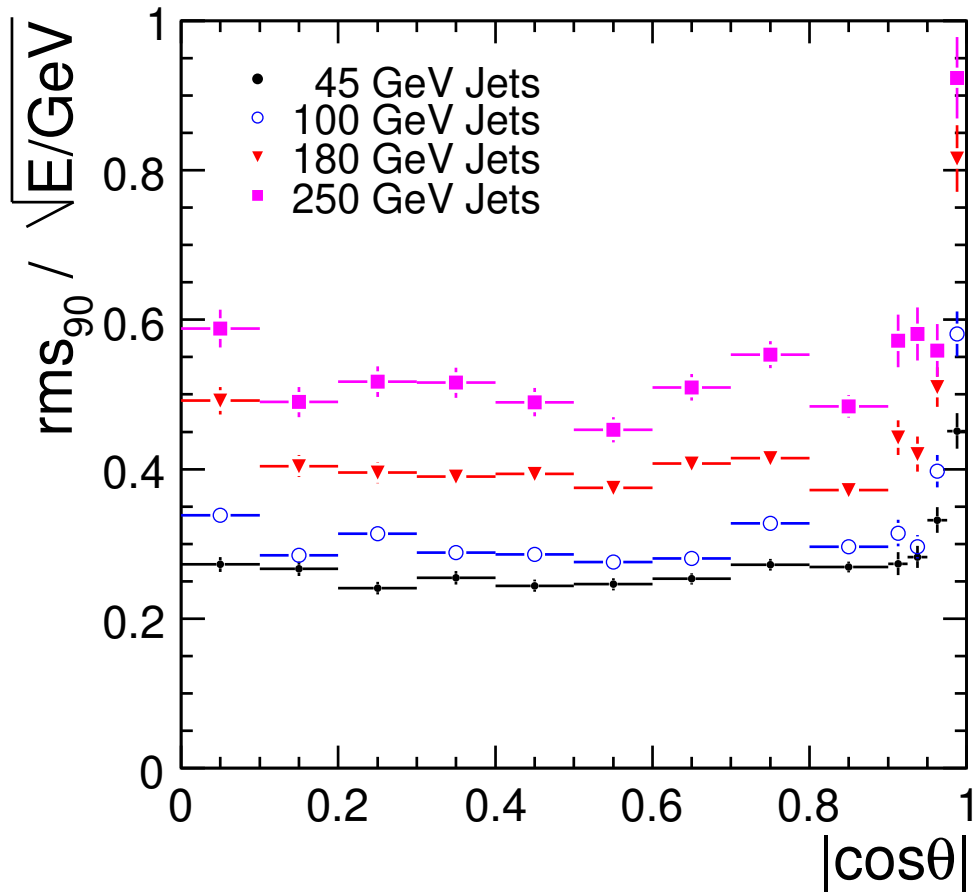


Figure 8: The jet energy resolution, defined as the  $\alpha$  in  $\sigma_E/E = \alpha/\sqrt{E(\text{GeV})}$ , plotted versus  $\cos\theta_{q\bar{q}}$  for four different values of  $\sqrt{s}$ . The plot shows the resolution obtained from  $(Z/\gamma)^* \rightarrow q\bar{q}$  events ( $q=u,d,s$ ) generated at rest.

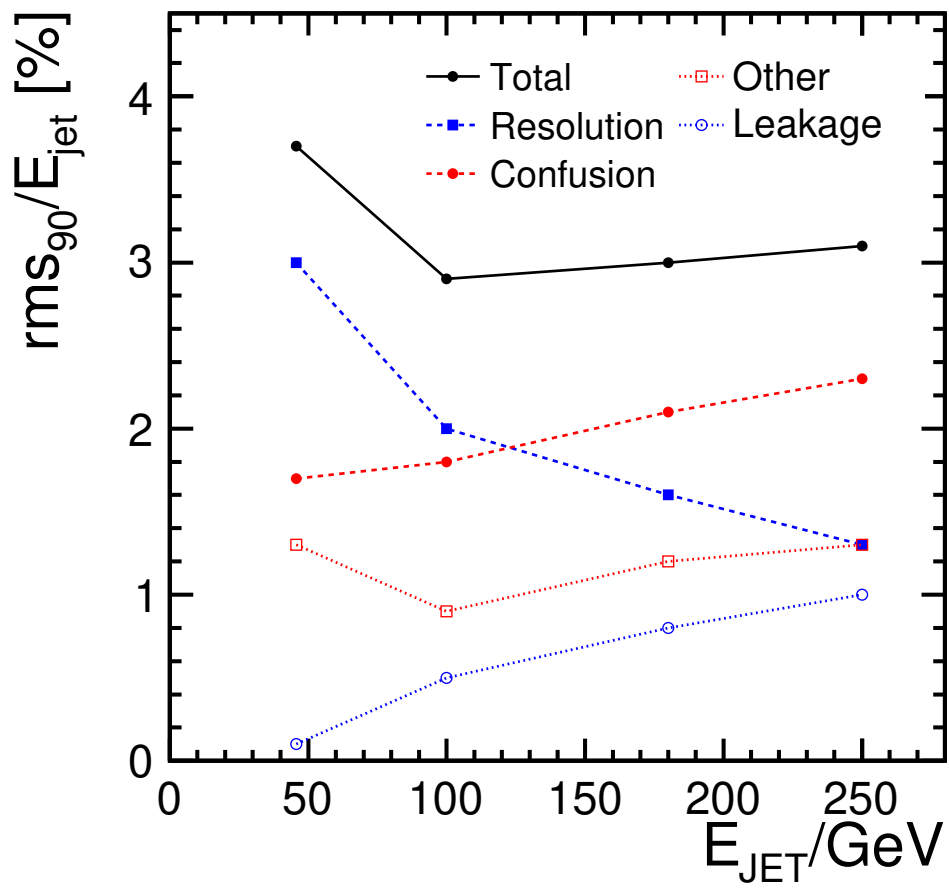


Figure 9: The contributions to the PFlow jet energy resolution obtained with PandoraPFA as a function of energy. The total is (approximately) the quadrature sum of the components.

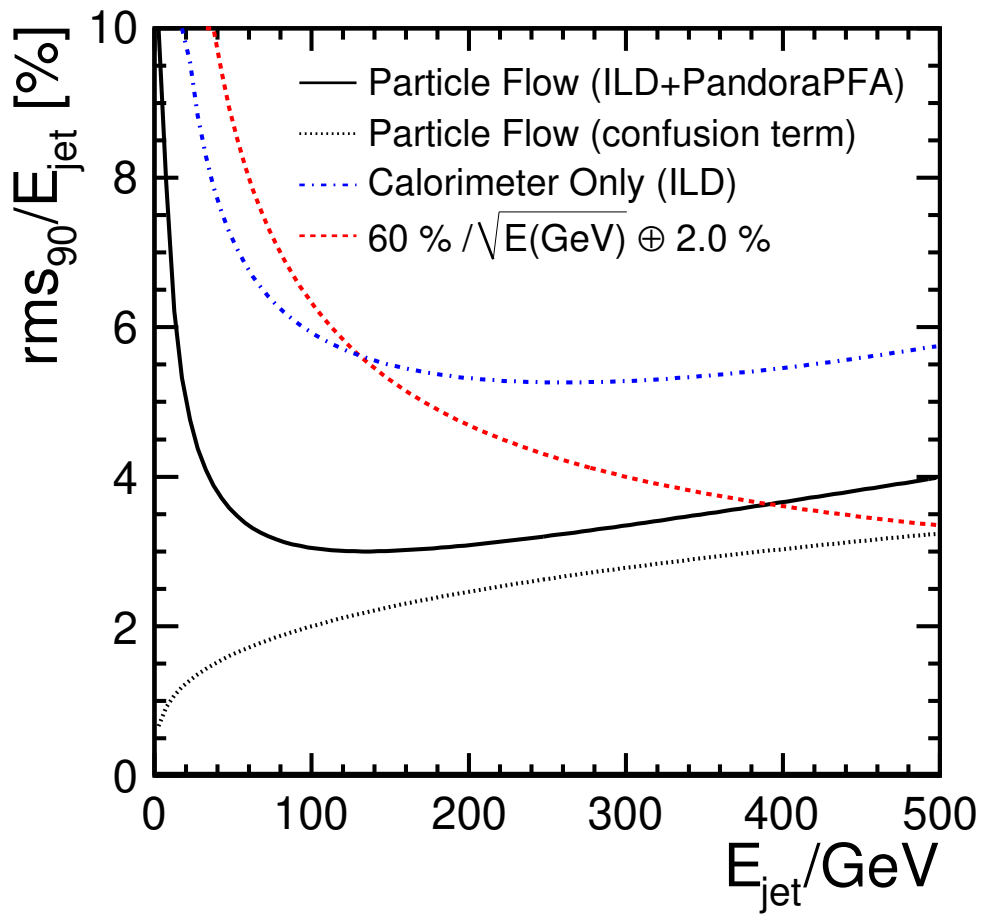


Figure 10: The empirical functional form of the jet energy resolution obtained from PFlow calorimetry (PandoraPFA and the ILD concept). The estimated contribution from the confusion term only is shown (dotted). The dot-dashed curve shows a parameterisation of the jet energy resolution obtained from the total calorimetric energy deposition in the ILD detector. In addition, the dashed curve,  $60\% / \sqrt{E(\text{GeV})} \oplus 2.0\%$ , is shown to give an indication of the resolution achievable using a traditional calorimetric approach.

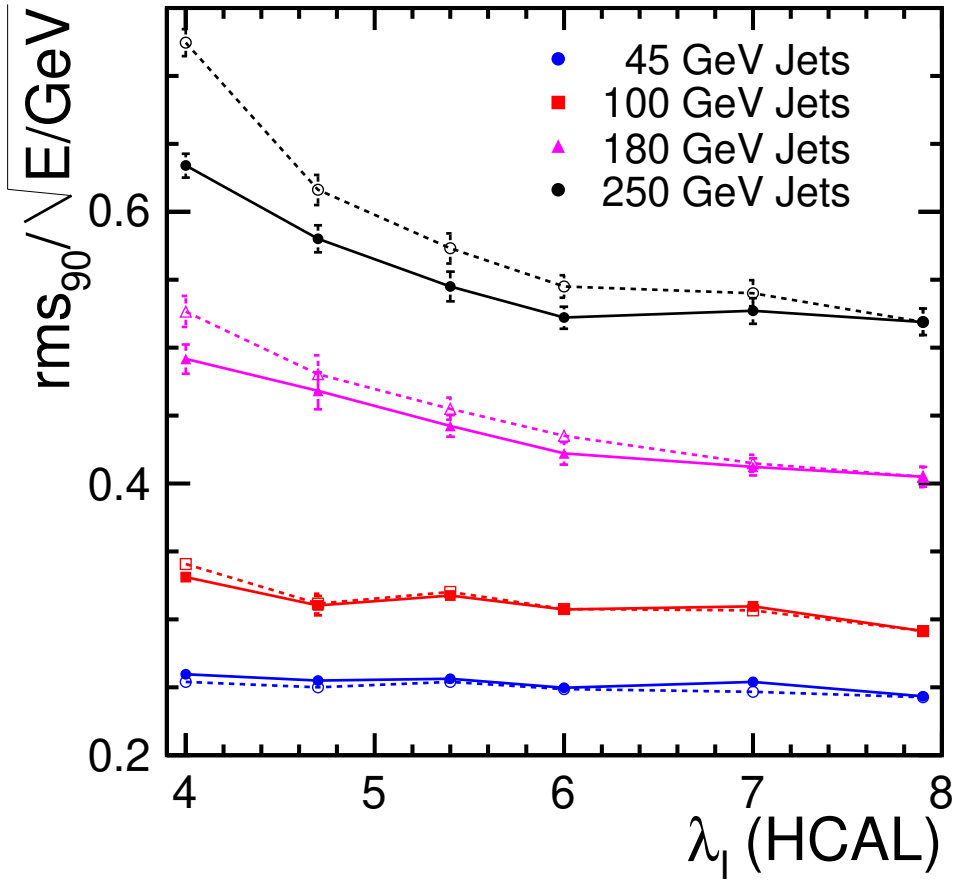


Figure 11: Jet energy resolutions ( $\text{rms}_{90}$ ) for the LDCPrime as a function of the thickness (normal incidence) of the HCAL. In addition, the ECAL contributes  $0.8\lambda_l$ . Results are shown with (solid markers) and without (open markers) taking into account energy depositions in the muon chambers. All results are based on  $Z \rightarrow u\bar{u}, d\bar{d}, s\bar{s}$  with generated polar angle in the barrel region of the detector,  $|\cos\theta_{q\bar{q}}| < 0.7$ .

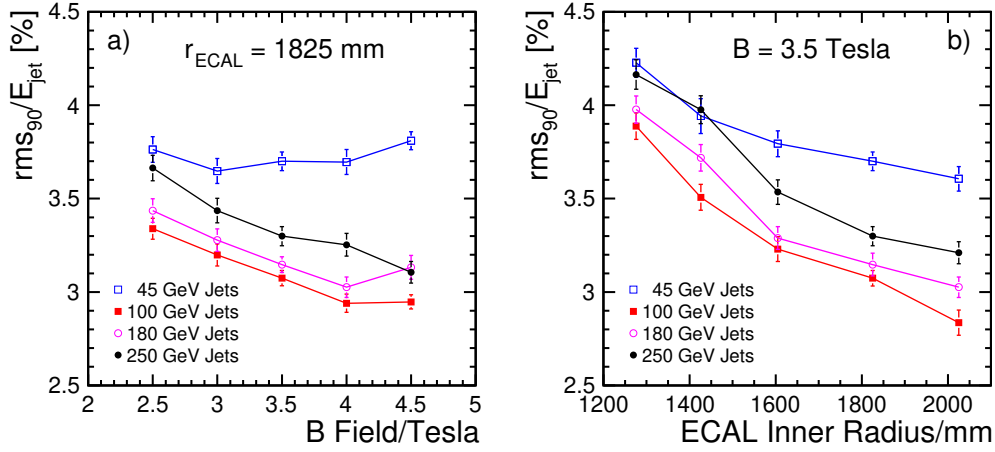


Figure 12: **a)** the dependence of the jet energy resolution ( $rms_{90}$ ) on the magnetic field for a fixed ECAL inner radius. **b)** the dependence of the jet energy resolution ( $rms_{90}$ ) on the ECAL inner radius a fixed value of the magnetic field. The resolutions are obtained from  $Z \rightarrow u\bar{u}, d\bar{d}, s\bar{s}$  decays at rest. The errors shown are statistical only.

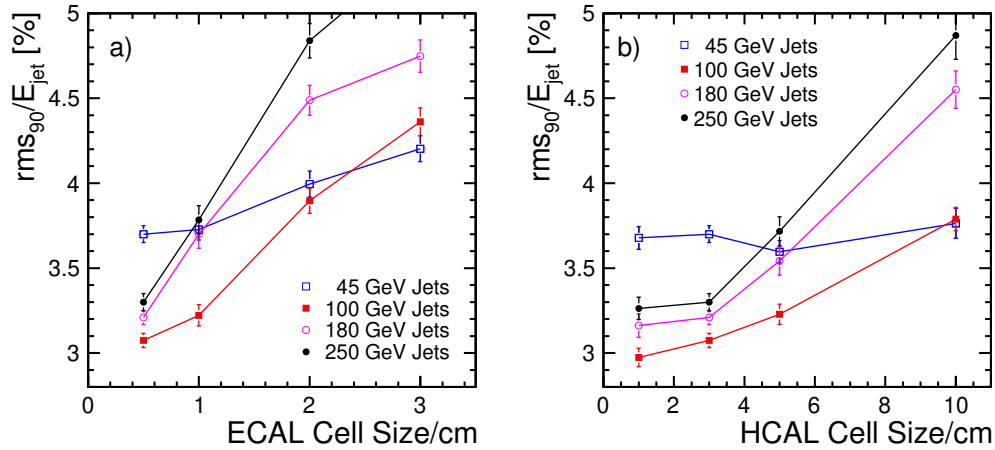


Figure 13: **a)** the dependence of the jet energy resolution ( $rms_{90}$ ) on the ECAL transverse segmentation (Silicon pixel size) in the LDCPrime model. **b)** the dependence of the jet energy resolution ( $rms_{90}$ ) on the HCAL transverse segmentation (scintillator tile size) in the LDCPrime model. The resolutions are obtained from  $Z \rightarrow u\bar{u}, d\bar{d}, s\bar{s}$  decays at rest. The errors shown are statistical only.

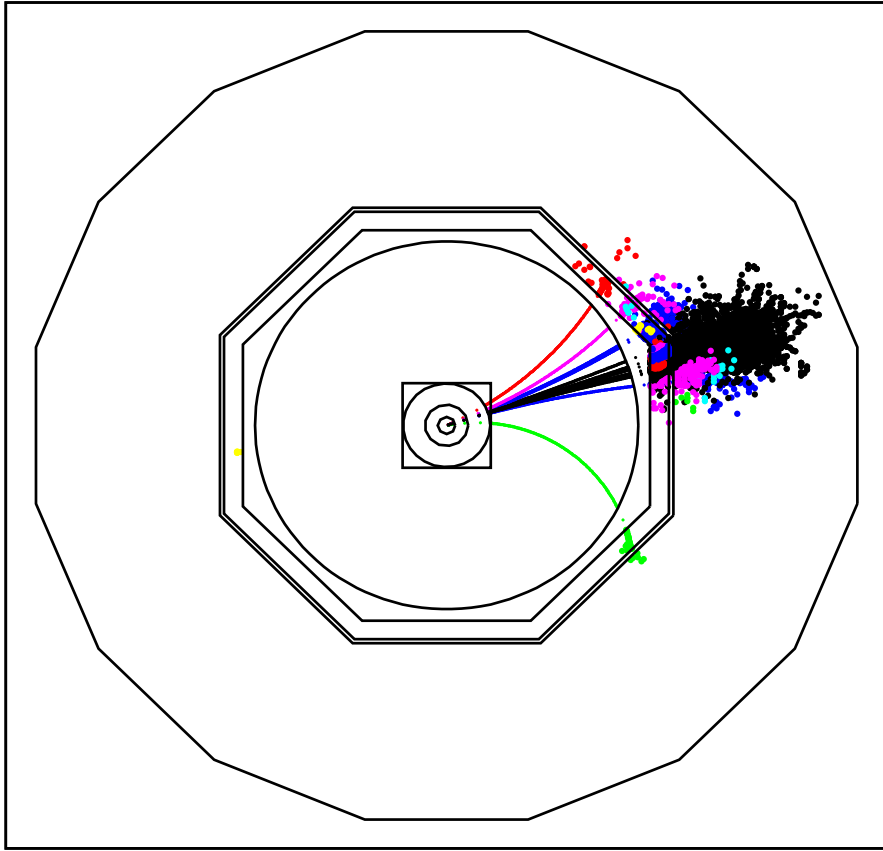


Figure 14: An example of a  $Z \rightarrow d\bar{d}$  decay with  $E_Z = 1 \text{ TeV}$  produced in a simulated  $e^+e^- \rightarrow ZZ \rightarrow \nu\bar{\nu}d\bar{d}$  interaction in the ILD detector concept.

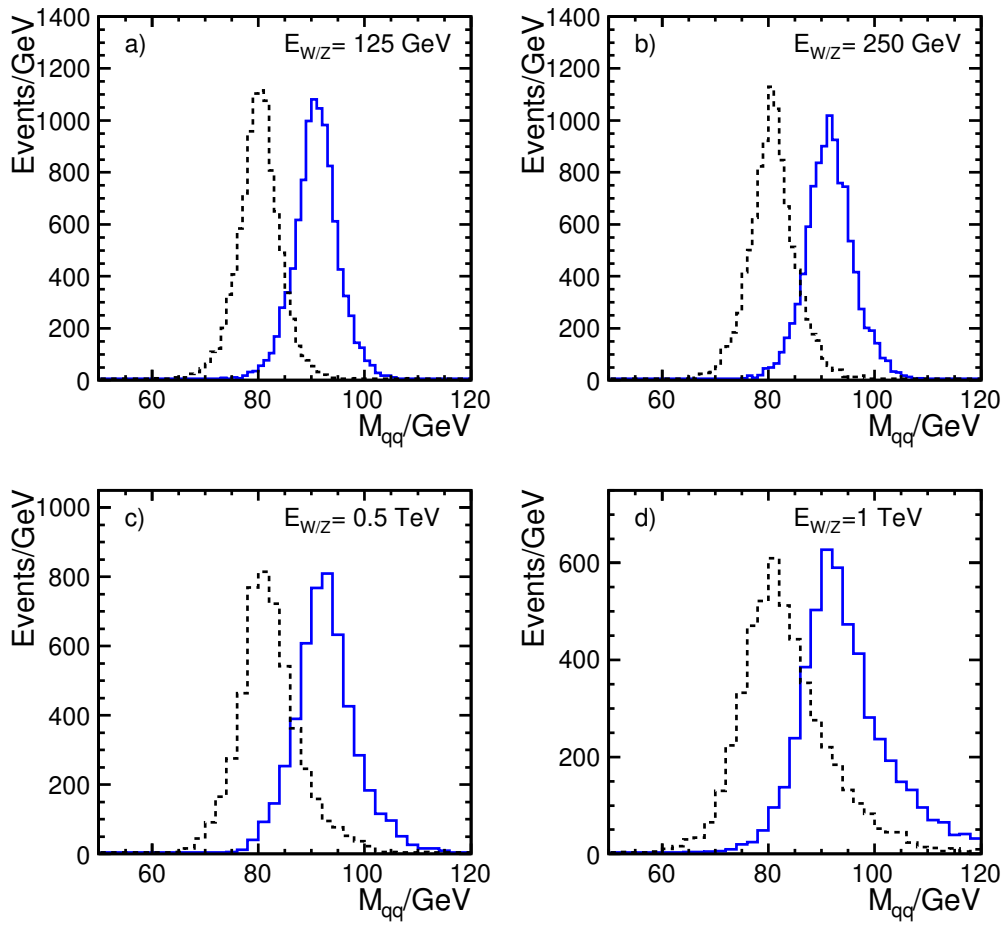


Figure 15: Reconstructed invariant mass distributions for the hadronic system in simulated  $ZZ \rightarrow \bar{d}d\bar{\nu}\nu$  and  $W^+W^- \rightarrow u\bar{d}\bar{\nu}\nu$  events as simulated in the modified ILD detector model.